# EFFECT OF PRESSURE ON THE PERFORMANCE OF ORGANIC LIGHT EMITTING DEVICES FABRICATED BY COLD WELDING

BY

ADENIJI, SHARAFADEEN ADETUNJI

A THESIS

SUBMITTED TO THE AFRICAN UNIVERSITY OF SCIENCE AND TECHNOLOGY

ABUJA – NIGERIA

IN PARTIAL FULFILLMENT OF THE REQUIREMENTS FOR THE

AWARD OF MASTER OF SCIENCE IN MATERIALS SCIENCE AND ENGINEERING

SUPERVISOR: PROF. W. O. SOBOYEJO

APRIL 2013

EFFECT OF PRESSURE ON THE PERFORMANCE OF ORGANIC LIGHT EMITTING DEVICES FABRICATED BY COLD WELDING

A THESIS APPROVED

BY

SUPERVISOR _____

PROF. W. O. SOBOYEJO

**DEDICATION**

*This work is dedicated to*

*my parents, Mrs Mojisola Simbiat and Mr Abduwahab ADENIJI,*

*my beloved wife, Omotayo,*

*and my dearest daughter, Fatima.*

*I love you all.*

## ACKNOWLEDGEMENT

First of all, I give thanks to almighty Allah for His mercy in my life. I also give thanks to my parents for their love, prayer, and supports. Most importantly, my mother, who is unlettered, but having recognized the importance of western education in life, she resolved that her children should be educated. This has been one the driving forces that motivates me to study, despite all odds, since my elementary school days. I pray that God spares your life and grant you sound health to reap the seed of the fruit you that you have sown.

My gratitude goes to the boards of Nelson Mandela Institution (NMI) and the African University of Science and Technology, (AUST) Abuja for the scholarship opportunity that was given to me to study at AUST. I promise I will never forget this kind gesture. It is my aspiration to give back to the university and the society at large in the nearest future as you have demonstrated to us.

My profound gratitude goes to my advisor, Prof Wole Soboyejo for his patience, trust and kindness towards, not only me, but every student. His excellent teaching methodology, open mind for discussions, and constructive suggestions have motivated me to improve myself and enjoy this work. My experience under his tutelage in the last eighteen-month has been wonderful. I am very grateful to you Prof. Wole. I also thank Dr. Omololu AKIN-OJO for his relentless effort, advice and evaluation of this work. Also, I appreciate every faculty member that has taught me in AUST.

I also appreciate my wife, Omotayo, for her understanding, endurance, and support, without which I wouldn't have been able to go this far. The appreciation is extended to my dearest daughter, Fatima Adedamola Abidemi. Your advent has been one of the most important things that have happened to me in this life as you are a blessed child.

My gratitude also goes to my dear friend, Iyiola, Olaniyi Samuel, who informed me about AUST and strongly encouraged me to write the entrance exams. Lastly, I appreciate my classmates: Funsho Kolawole, Abimbola Adedeji, Elijah Jossou, Tunji Adetayo Owoseni, Odette Ngasho, Amine Ilboudo, Adeyinka Idowu, Fortunatus Jacob, Ifeanyi Kalu, and Deborah Olalekan. You are all wonderful!

## ABSTRACT

Analytical and finite element models were used to simulate additive cold welding patterning processes. The effects of adhesion, pressure, thin film (layer) thickness and dust particle modulus (between the contacting surfaces) are examined. A simple model is developed and used to determine the contact profiles around impurities between cold-welded thin films. These are computed as a function of adhesion, particle modulus, and layer thickness. The models are shown to provide new insights into the significance of adhesion, layer thickness and particle modulus in the surface contacts that occur during cold welding. The implications of the results are then discussed for the design and fabrication organic electronics via cold welding.

**TABLE OF CONTENTS**

## LIST OF FIGURES

## LIST OF TABLES

# Chapter 1 Background and Introduction

## 1.1 Introduction

Light-emitting diodes (LEDs) are optoelectronic devices that generate light when they are electronically biased in the forward direction. The early commercial LEDs devices, in 1960s, were based on inorganic semiconductors such as gallium arsenide phosphide (GaAsP) as an emitter and their efficiencies were very low [1]. After 40 years of development, the efficiencies of inorganic LEDs have been significantly improved and they are used in a wide range of applications such as telecommunications, indicator lights, and more recently in solid-state lighting. The applications of LEDs have been very limited for flat panel displays. High-resolution pixelated LED arrays are very expensive to fabricate and the application of LEDs in displays has been limited to bill board displays where individual LEDs are manually mounted on the display boards.

The light-emitting diodes that are made with organic materials are called organic light emitting diodes (OLEDs). Prior to the invention of OLEDs, organic-based devices could only be operated in electroluminescence mode. The first organic electroluminescence device was demonstrated in 1960s, and very high operating voltages were required [1]. These devices were made with anthracene single crystals doped with tetracene (a blue-emitting fluorescence dye) sandwiching between two electrodes. Very high voltages were required and the efficiencies were very low. In the 1980s, a major breakthrough was made as low-voltage OLEDs were demonstrated. In contrast to the first electroluminescence devices, the new OLEDs devices were based on a multilayer structure and they consisted of a transparent anode, a hole transporting layer, an electron emitting layer, and a cathode. During operation, electrons and holes are injected from a cathode and an anode, respectively, and recombination of electrons and holes leads to efficient light generation.

There have been several efforts to improve the lifetimes and efficiencies of these devices [2] as well as efforts to implement low cost processing techniques that take advantage of the material properties of these devices [3, 4]. These efforts have produced varying amounts of successes which have resulted in the commercialization of organic electronic devices in hand held displays [5] among other applications.

Even though it is possible to create a pattern of this device on the nanoscale using the same lithographic-based techniques used in microelectronics provided radiation of an appropriate wavelength is available, such scaling-down approaches have significant drawbacks. For instance, in the realization of advanced organic electronic devices, many organic materials degrade when exposed to solvents or aqueous chemicals, making conventional photoresist processing problematic [6]. Other patterning methods, such as shadow-masking [7] suffer from low pattern resolution. Recently, several new techniques have been developed for the fabrication of nanoscale electronic devices [8] that strive to overcome the limitations in conventional methods while at the same time providing improved spatial resolution. Such an example is direct micro and nanopatterning [9] by cold welding.

Cold welding has attracted widespread attention as a potential low-cost approach, especially for the fabrication of organic electronic devices [10]. In the cold-welding patterning process, a stamp is brought into contact with a substrate upon which a very thin metal layer has been deposited. The contact results in the formation of strong or cold-welded bonds between the stamp and the thin layer [11]. When the stamp is retracted from the substrate in the subtractive process, material from the substrate adheres to the stamp, leaving behind a patterned film/substrate. On the other hand, when the stamp is withdrawn in the additive process, it leaves material originally on the stamp on the substrate. The essential parts of this process include adhesion and the contact of the thin film in the presence of dust particles. Both are important in determining the final resolution as well as the mechanical robustness of

the resultant pattern in a way that provides the basis for the most optimized design of efficient and long-lived devices.

## 1.2 Research Objectives

There are still significant unresolved issues that must be resolved to enable the design of improved contact and adhesion between multilayers that are relevant to organic thin-film electronic devices. The objectives of the current work are to:

(i) Identify the effect of processing condition such as pressure on the device in the presence of dust particles;

(ii) Study the effect of dust particles' moduli on the contact profiles in a way that gives new insights into the contact and adhesion phenomena during cold-welding

(iii) Investigate the effects of layer thickness on the contact length in the vicinity of dust particle that occurs in clean room during cold-welding

## 1.3 Scope and Organization

In this work we focus on additive cold welding patterning process. The quantities of interest in this process include; the contact length as a function of dust particle size, film thicknesses, and the effects of dust particles' moduli on the adhesion and contact between the two layers in contact. The dust particles in the clean room have been shown to play a key role in the contact and adhesion between cold welded surfaces [10]. We, therefore, focus on understanding the performance of the OLEDs at various dust particles' moduli, pressure values and film thicknesses. We performed both analytical and continuum finite element analyses (FEA) to mimic the additive cold-welding patterning process in order to study the interaction between the layers.

In our approach, a thin film of Ag lies on top of a flat substrate and a thin film of Au sits on a flexible stamp with a finite pattern. These signify the silver and gold layers respectively, and dust particle is considered to be present in between the two layers. The substrate is fixed while the stamp is pressed against it by the application of pressure in order to form the Au-Ag interface. The arrangement was also reversed in order to form Ag-Au interface. If the work of adhesion, geometric and the mechanical properties of the films are appropriate, retraction of the stamp leaves a section of the film via some localized material failure mechanism on the substrate. Our modeling and simulations consider the effect of film thickness, dust particle modulus, work of adhesion and pressure on the performance of the device. Hence, we develop a simple model to quantify the performance of the OLEDs, as an explicit function of the pressure, particle's modulus, film thickness, and the dust particle size.

Chapters 1 and 2 present the introduction and literature review, respectively. The analytical and continuum finite element analyses (FEA) were presented in chapter 3 while chapter 4 contains the results, discussions and implications. Conclusion and recommendations for future works are presented in Chapter 5.

## References


1. Sam-Shajing Sun, “Introduction to Organic Electronics and Optoelectronic Materials and Devices” (2008)
2. C. Woong et al, “Improved device performances in polymer light-emitting diodes using a stamp transfer printing process”, Organic Electronics, Volume 10, Issue 2, 2009, Pages 372-375, (2009).
3. Alexey N. Krasnov, “High-contrast organic light-emitting diodes on flexible substrates”, Appl. Phys. Lett. 80, 3853 (2002).
4. C. Kim et al; Yifang Cao; Soboyejo, W.O.; “Forrest, S.R., "Fabrication of organic light-emitting devices by direct transfer of active organic materials using organic-organic adhesion," The 17th Annual Meeting of the IEEE Lasers and Electro-Optics Society, Vol.1, pp. 336-337 (2004).
5. J. M. Shaw and P. F. Seidler, “Organic Electronics: Introduction,” IBM J. Res. & Dev., 45, no. 1, 3–9 (2001).
6. J. Song, D. J. Srolovitz “Molecular Dynamic Investigation of Patterning via Cold welding,” J. Mech. Phys. Solids 57 (2009) 776-787.
7. Tian, P.F., Burrows, P.E., Forrest, S.R., (1997). Photolithographic patterning of vacuum-deposited organic light emitting devices. Applied Physics Letters 71 (22), 3197–3199.
8. Didiot, C., Fagot-Revurat, Y., Pons, S., Kierren, B., Malterre, D., Tejeda, A., Rousset, S., (2007). Electronic properties of (Co, Ag) self-organized nano dots on Au(111) vicinal surfaces. Applied Surface Science 254 (1), 45–49.
9. Kim, C., Burrows, P.E., Forrest, S.R., (2000). Micropatterning of organic electronic devices by cold-welding. Science 288 (5467), 831–833.

10. C. Kim and S. R. Forrest, “Fabrication of Organic-Light Emitting Devices by Low Pressure Cold Welding,” Advanced Materials, 15, no. 6, 541-545, (2003).
11. Alcantar, N.A., Park, C., Pan, J.M., Israelachvili, J.N., (2003). Adhesion and coalescence of ductile metal surfaces and nanoparticles. Acta Materialia 51 (1), 31–47.

# Chapter 2

## Literature Review

### 2.1 Structure of small organic molecule LEDs

Organic light emitting diodes consist of sequence of organic layers between two electrodes; an anode for hole injection and a cathode for electron injection. The layers and there basic functions are shown schematically in Figure 2.1 below:

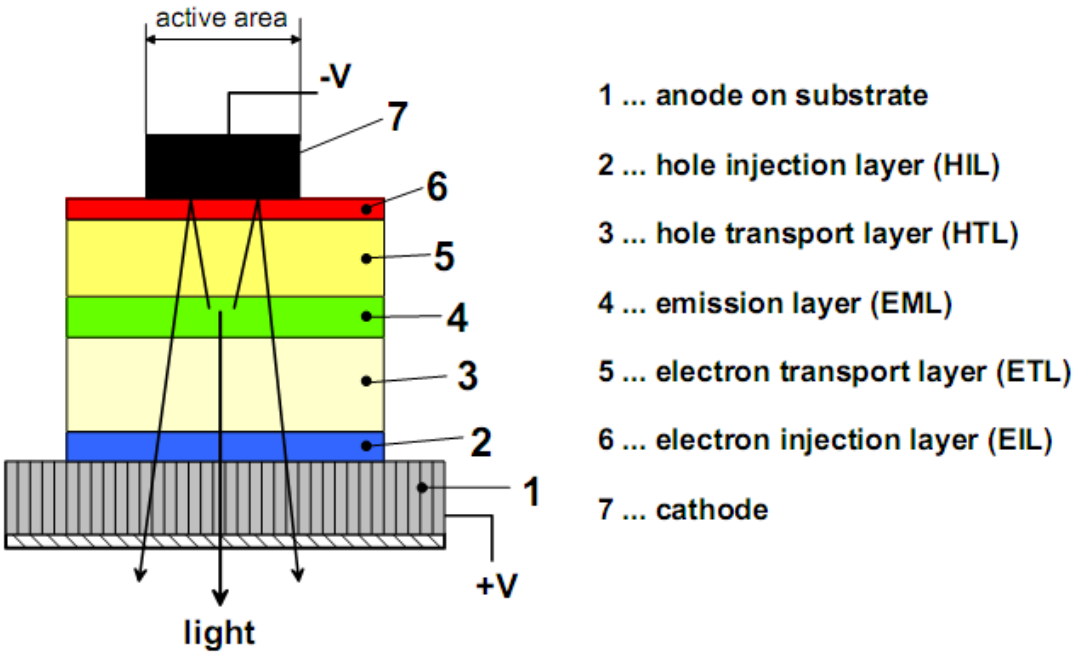


Figure 2.1: Principle layer sequence of an OLED and basic function of each layer (adapted from Zur et al. 2001 [1])

When the device is positively biased, holes are injected from the anode and electrons from the cathode. The charge carriers drift through the transport layers and meet in the emission layer. The charge carriers form excitons (neutral excited states or bound electron-hole pairs) at the emission layer, which show a certain probability to decay radiatively.

In order to attain a high efficiency which is a function of emitted photons per injected electrons, the layers need to fulfill certain requirements. The hole injection layer (HIL) has to facilitate hole injection from the anode into the hole transport layer (HTL). This could be achieved by choosing the energetic level of the highest occupied molecular orbital (HOMO) to be in between the HOMO of the HTL and the ionization potential of the anode [1]. This is illustrated in Figure 2.2. The HOMO and lowest unoccupied molecular level (LUMO) levels are analogous to the valence and conduction bands in inorganic semiconductors and the vacuum level is assumed to be aligned. The hole transport layer should have a high hole mobility and must be able to obstruct electrons emanating from the cathode from reaching the anode, as this could result into a 'shunt' current.

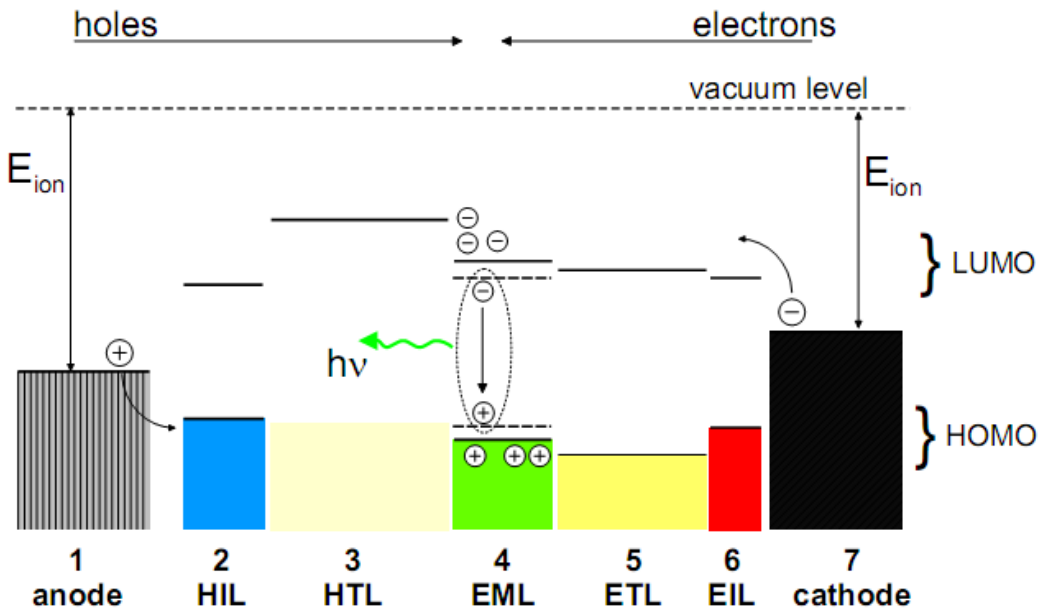


Figure 2.2: Schematic view on a favorable energetic situation in an OLED

Also, the transmission of the organic layers should be high in the emission wavelength region. The HOMO and LUMO positions of the emission layer (EML) should enhance hole and electron injections from the neighboring layers. In addition, the photoluminescence efficiency (which is the ratio of radiatively recombining excitons to created excitons) of the

emissive material should be high and the emission should be red-shifted to the absorption (Stokes-shift). The properties of the electron transport (ETL) and electron injection (EIL) layers should be complementary to those of the HIL and HTL [2]. In other words, a suitable LUMO level should be chosen with high electron mobility. Since the anode needs to have a high ionization potential to inject holes into the HOMO of the HIL, then, the cathode should be a low work-function metal. Meanwhile, at least one of electrodes must be transparent for visible light in order to achieve a high light outcoupling efficiency. This is why indium-tin-oxide (ITO) is used as transparent anode in most cases.

### 2.2 The development of organic light-emitting diodes

The first electroluminescence organic semiconducting materials were realized in 1960s [2, 3]. Pope et al. in 1963, [2] observed electroluminescence in small molecule of organics in their earlier work. One of notable achievements at that period was the work of Helfrich et al. [4] which solved the problem of electron injection into the organic material (at that time only the hole injection from a solution of potassium-iodine was efficient) by using a solution of negative anthracene ions. This became the first experimental proof that electroluminescence needs bipolar charge injection into the device, the capture of oppositely charged carriers in a recombination zone and the radiative decay of the thus created excited electron-hole pairs (excitons). However, the recombination efficiency was rather low.

This was followed by the work of Tang and Van Slyke [3] that constructed electroluminescent device using organic molecules. Their electroluminescence device is still the prototype for today's highly developed OLEDs. It consisted of the hole injection contact indium-tin-oxide (ITO), which is a highly doped transparent inorganic semiconductor, an aromatic diamine (TPD) as hole transport material, an emissive layer of aluminium-tris-(8-hydroxy-quinolate) (Alq3) and a magnesium-silver alloy (Mg:Ag) as electron injection

contact. All layers were sublimed in a vacuum system and were amorphous. The success of this diode can be attributed to the superior choice of the materials involved: (1) Alq3 shows a high photoluminescence-efficiency which is strongly red shifted to the absorption; (2) the diamine layer keeps the emission zone away from the light-quenching contacts, and (3) ITO and Mg:Ag show efficient injection of holes and electrons, respectively, into the neighboring organic layers. Despite the fact that ITO and Alq3 exhibit disadvantages in terms of stability, these materials are still widely used for organic light emitting diodes. The LED of 1987 needed 5.5V to reach a luminance of 100 cd/$m^2$ (common monitor and cathode-ray-tube brightness) and had a current efficiency of approximately 2 cd/A [1]. The green emission originates from the Alq3 layer. This breakthrough in device efficiency and operating voltage was the take-off for intense research on organic semiconductors and their use for organic light-emitting diodes.

In 1990, Burroughes et al. [5] from the Cambridge group followed up with a highly efficient OLED based on polymers (PLEDs). The prototype emitter material in their work was poly(p-phenylene-vinylene) (PPV), which, similar to Alq3, emits in the green wavelength region. Since then, there have been several studies of methods for the fabrication of organic light emitting diodes (OLEDs) and other organic electronic devices. These have been explored as low-cost alternatives to traditional silicon-based devices. Although the field of organic electronics is relatively new, compared to that of silicon electronics, the performance improvements in OLEDs and in organic conducting/semiconducting materials have already generated great commercial interest [6].

There are several unconventional methods for the fabrication of OLEDs and other organic electronic devices. A series of soft lithography methods for the micro- and nanofabrication of organic polymeric materials was reviewed by Xia et al. [7–9]. Soft lithography (Figure 2.3)

stands for several patterning techniques such as: replica molding (REM), microcontact printing (μCP), micromolding in capillaries (MIMIC), microtransfer molding (μTM), solvent-assisted micromolding (SAMIM), and near field conformal photolithography. All these techniques use a patterned elastomer, usually PDMS, as the mold. A stamp or mask is used to generate or transfer the pattern. Soft lithography has obvious advantages over photolithography and other conventional microfabrication techniques for the patterning of non-planar substrates, unusual materials, or large-area structures. It is especially promising for the microfabrication of relatively simple, single-layer structures, for uses as sensors, micro-analytical systems, in MEMS, and in applied optics [7].

Stamping is a technique that is similar to additive cold welding. In this technique, a stamp is also used to transfer one material onto the other. A self-assembled monolayer is also usually included between the stamp and the coating to reduce the adhesion between them. It is also used to facilitate the easy transfer of the coated material to the substrate.

The difference between this technique and the cold welding technique is that: (1) at least one of the transferred material and the substrate material is organic polymer and (2) those two materials are joined together by the adhesion between them. This method has been used by Rhee and Lee [10], who applied pressure to a metal coated stamp. This was used to transfer the metallic cathode onto the organic active layer of OLEDs, as shown in Figure 2.2 (a). The stamping has also been used by Kim et al [10] to transfer the active organic layer in OLEDs to an organic strike layer. This was achieved by utilizing the adhesion interactions between different organic layers within the OLEDs, as shown in Figure 2.4 (b). In a similar manner, Joo et al. [11] used stamping to transfer active organic layers to ITO-coated glass substrates that were used to fabricate polymer light emitting diodes (PLEDs).

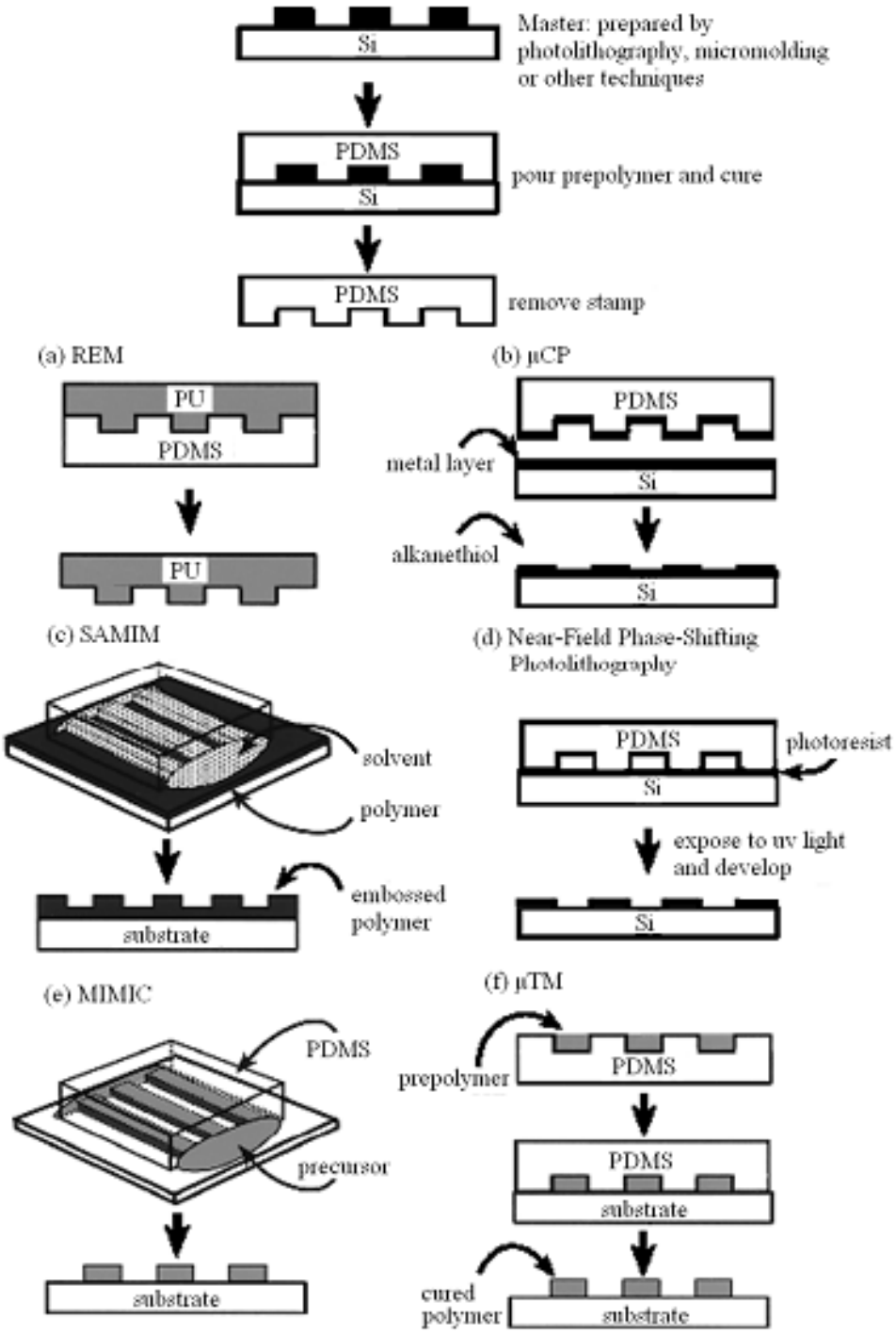


Figure 2.3: Schematics of several soft lithographic methods [7]: (A) replica molding (REM), (B) microcontact printing (μCP), (C) solvent-assisted micromolding (SAMIM), (D) near field conformal photolithography, (E) micromolding in capillaries (MIMIC), and (F) microtransfer molding (μTM).

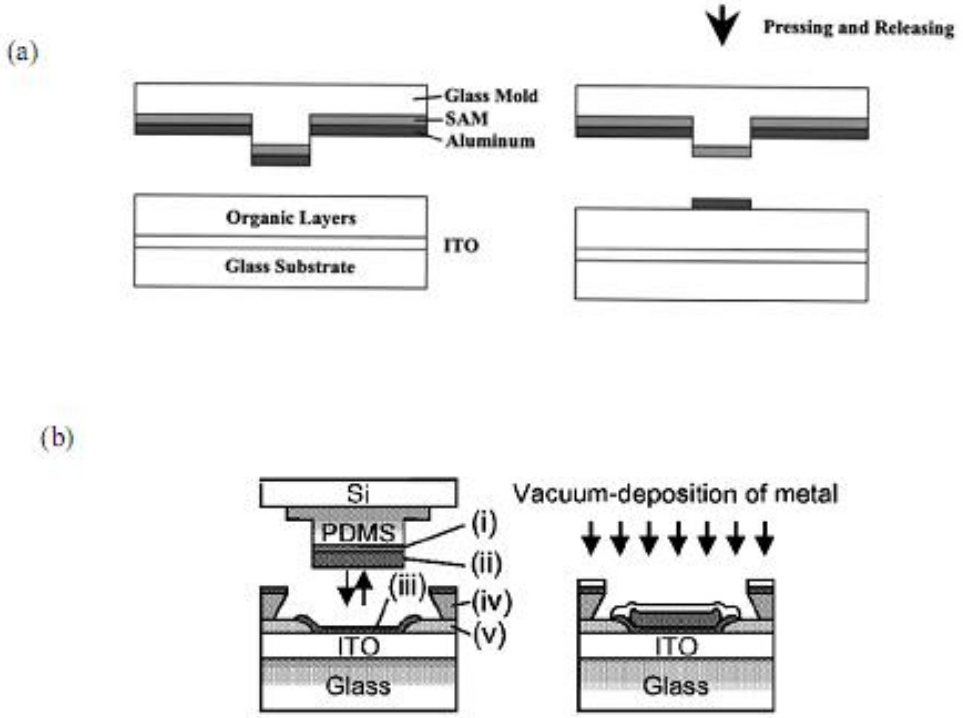


(i) Adhesion reduction layer, (ii) Alq3/α-NPD layer, (iii) α-NPD strike layer, (iv) Overhang structure, (v) Insulating layer.

Figures 2.4: Schematics of stamping of (a) a metal cathode onto an organic layer [10] and (b) an organic active layer onto another organic layer [12] in the fabrication of OLED.

Lamination is another organic electronic fabrication technique. Instead of transferring materials from one place to another, it brings several layers of materials together into optimal contact to form the devices. Lee et al. [13] illustrated a soft contact lamination method, as shown in Figure 2.5 (a). The patterned OLEDs were built by bringing a patterned metallic electrode layer on a flat elastomer substrate and the active organic layers on an ITO glass substrate into contact. The homogeneous and intimate contact relied only on van der Waals interactions. It is therefore, achieved without applying heat or pressure.

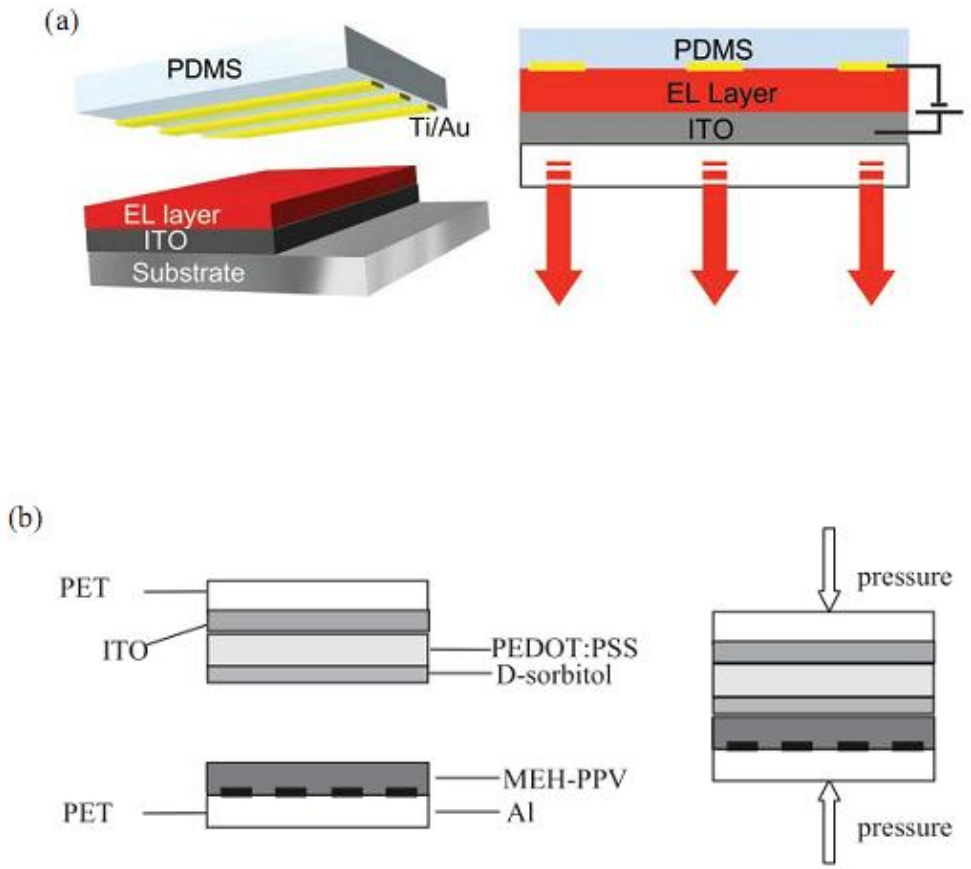


Figure 2.5: Lamination method and its applications in (a) soft contact lamination of OLEDs [13], (b) electric glue assisted lamination of OLEDs [14].

Ouyang et al. [14] fabricated a polymer light-emitting diode using a lamination process in which the adhesion was facilitated by a conducting polymer. The latter was used as transparent electric glue (Figure. 2.5(b)). The integration of organic thin-film transistors (OTFTs) and OLEDs have been considered as a promising technology for high-resolution flat panel displays and solid state ligthing in which OLEDs can be operated by the OTFTs. Zyung et. al. [15] fabricated such structure using a lamination method. The OLED and the OTFT were first fabricated separately on plastic substrates. Both devices were then, laminated using silver paste that acts, as not only as the adhesive, but also as the electric connector between the drain electrodes of the OTFT and the anode of the OLED. Liu et al. [16] also used this

method to fabricate similar active OLED structures, driven by TFTs, that enabled top emission using bottom-emitting OLED. Moreover, the lamination process has been used by Kim et al. [17] in the encapsulation of OLEDs. This was done by laminating an adhesive multilayer of polyacrylate-based adhesive layer and aluminum passivation layer on to the devices to prevent degradation of the device.

The performance of organic electronic devices fabricated by the above fabrication methods has been reported to be better than those of the devices fabricated by conventional methods [11], [13]. The performances of spin-coated and stamped devices have been compared by Joo et al. [11]. They showed that the morphologies of the spin-coated and stamped devices are similar. However, the stamped devices were better than the spin-coated devices in terms of current density, light-emitting efficiency and lifetime. In particular, the lifetimes of the stamped device was doubled compared with that of the spin-coated device.

Even for those devices fabricated by conventional methods, such as chemical vapor deposition, Kim et al. [18] demonstrated a compression treatment similar to the above unconventional fabrication methods. By applying and releasing physical pressure to the devices, a notable increase was observed in the performances of the devices. These include improvements in luminance intensity and current efficiency. Larger pressure led to better performance. They argued that the improvement was due to more intimate contact between the organic molecules in the organic layer.

### 2.3 Cold Welding

Cold welding or cold pressure welding is the process by which clean, oxide free metallic surfaces are brought together to achieve intimate contact, and thereby form metallic bonds [19]. The process is termed a “cold” weld because the bonding mechanism is achieved at room temperature. For optimal results, the metal surfaces chosen need to have similar crystal

structure and atomic radii [20]. For very reactive metals, the oxides formed on exposure to air have to be brittle enough for the underlying metal to plastically deform through the cracked-oxide, in order to form the cold weld junction [21].

The patterning of metal electrodes by cold welding, reported by Kim et al. [8, 22], provides a good opportunity for the realization of post-deposition electrode patterning (i. e. the patterning of a metal film after an organic layer is deposited). This method is based on the transfer of a thin film of metal between substrate and stamp, using a cold welding process. This patterning technique can be implemented under ambient conditions and also in a vacuum [23]. Kim et al. [22] have elaborated the potential to extend the cold welding technique to ultimately result in the printing of large-area organic electronic circuits using roll-to-roll methods, in which the devices are fabricated in a continuous, high-speed, low-cost process. Xu et al. [24] has also used the cold-welding processes to enable the direct transfer of metals onto pre-formed hemispheres with micrometer scale feature resolution. This was used to realize 10 kilopixel organic photodetector focal plane arrays (FPAs) that mimic the size, function, and architecture of the human eye.

In the additive cold welding as shown in Figure 2.6, a metal coating is deposited onto a pre-patterned stamp, which is then brought into contact with a substrate with a very thin metal "strike-layer" of similar composition to the layer on the stamp [25]. The contact results in the formation of strong metallic or cold-welded bonds [26, 27] between the two clean metal surfaces. The separation of the stamp from the substrate leaves the stamp metal on the substrate only in the desired contact regions. In the subtractive cold-welding process (Figure 2.7), the cold welding process and the delamination occurred on a stamp rather than on a substrate.

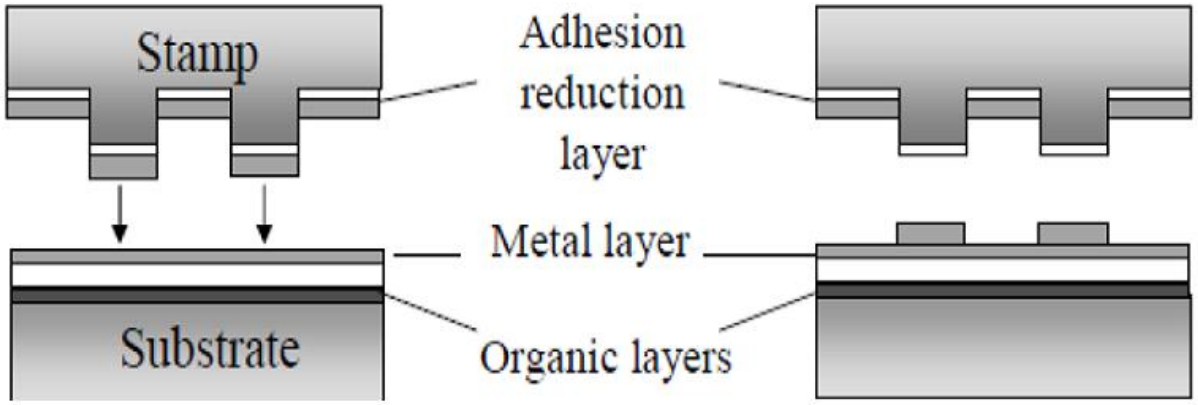


Figure 2.6: Patterning of Electrode by Additive Cold-Welding Technique [28]

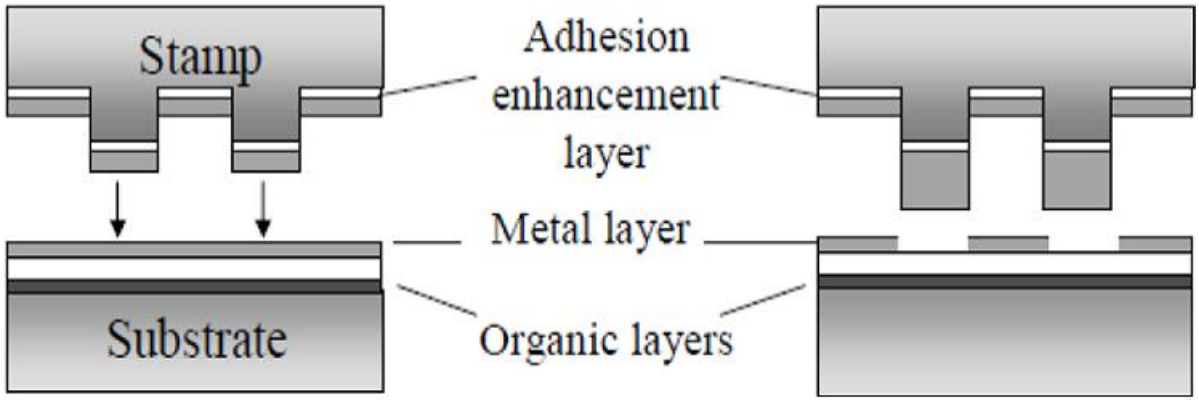


Figure 2.7: Patterning of Electrode by Subtractive Cold-Welding Technique [28]

Thus, the required pressure (>>150MPa) was significantly reduced compared to that for the additive method (>>300MPa) [28]. However, the high pressure levels required for the transfer of the metal layers is still the remaining problem of the cold welding technique. For example, during the source and drain patterning of pentacene, organic thin film transistors (OTFTs), the pentacene was occasionally wrinkled as a result of high shear stress at the pentacene – insulator interface [28]. Sink-in of dust particles and deformation of layers may also result in damage within the devices fabricated by cold welding.

Apart from electrode patterning, cold welding has been used in industrial manufacturing process. Such applications have motivated metallurgical studies of joint microstructures and

mechanical properties [29, 30]. In addition to device patterning, most recently, cold welding has been used as a general method for micro-scale fabrication. It has also been used to fabricate nano-scale mixing chambers for micro fluidic devices [32], as well as microelectronic packages [33], as shown in Figure 1.3. Such smaller-scaled applications have stimulated recent studies of cold welding physics in which dust particles in the clean room have been shown to play a key role in the contact/adhesion between cold welded surfaces [34].

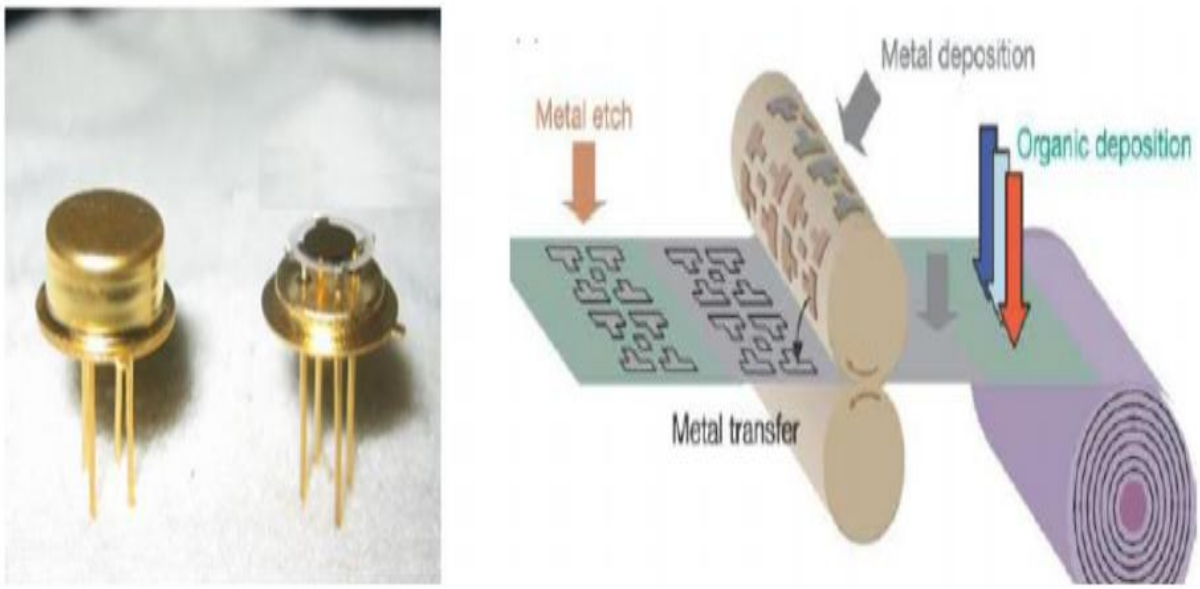


Fig.2.8: Application of Cold Welding: (a) Micro Electronic Packaging (b) Roll-to-Roll fabrication of organic Electronic Devices (Sources: (a) Precision Devices (b) USAMI)

However, our understanding of the contact profiles and dust particles is still limited. Prior work done by Cao [34] used finite element analyses to estimate the lengths in the vicinity of dust particles that are present in clean room environment. The work was instrumental in predicting lower, but sufficient pressure levels, that enabled adequate contact using lower modulus stamps. Indeed, by using flexible poly (dimethyl-siloxane) (PDMS) stamps, Kim and, Forrest [25] found that cold welding of gold layers can be used to fabricate organic light emitting devices at pressure, 1000 times lower than those required using rigid silicon stamp [24].

Subsequent experimental work by Cao et al. [36] and Akande et al. [37] revealed the role interfacial impurities, i.e. dust particles, at the cold-welded interfaces between Au and Ag thin films. They also developed a theoretical model to predict the contact profiles around impurities between cold-welded surfaces. These provided new insights into how adhesion affects the surface contacts that occur during cold welding.

Meanwhile, the Cao et al [36] analyses did not include the effects of adhesion forces between the interacting Au and Au layers. This was because there was no general method of including the effects of adhesion numerically within the finite element framework [37]. Since such adhesion forces can be quite significant, Akande [37] presented an accessible model that can relate the dust particle sizes and adhesive forces to the contact profiles that can occur around dust particles between layers that are being joined together. The results from both experimental and theoretical work were presented which include the effect of adhesion forces between the interacting Au and Ag layers.

## 2.4 Dust Particles and Interfaces

Transmission Electron Microscopy (TEM) images showing the microstructures and interfaces of as deposited and cold welded Au-Ag thin films are presented in Figure 2.9. These show, clearly, that there is a significant difference between the as deposited and cold-welded interfaces. The as-deposited interface has a wavy morphology, largely due to surface roughness. In addition to the waviness, some large irregularities or voids are observed along the cold-welded interface [37].

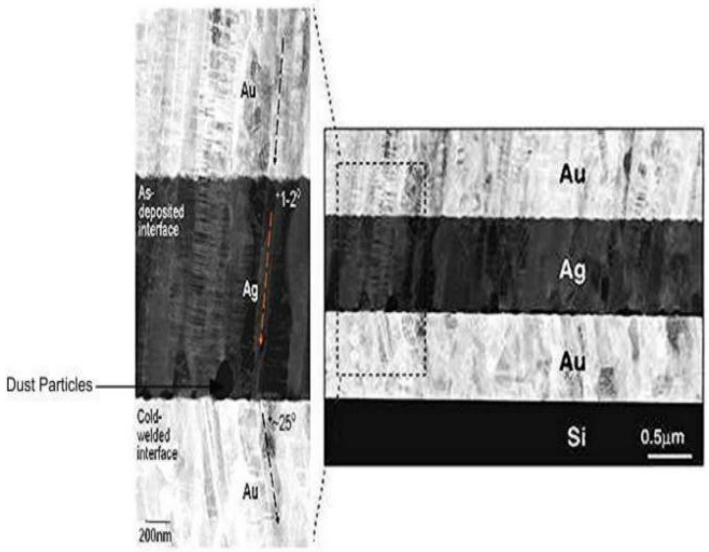


Figure 2.9: TEM images showing interfaces of as deposited and cold-welded Ag-Au thin film [37]

Significant large voids, with heights between 40-160 nm, were found along the cold-welded interface, (Figure 2.9). Considering that typically formed micro-voids are due largely to asperity profiles and their subsequent deformation. Hence, the voids observed here cannot be attributed to surface roughness alone. Instead, larger voids are associated with dust particles that were embedded between the two surfaces during cold welding. These dust particles amplify the void sizes observed at the cold welded interfaces, as suggested by Akande [37]. Typical dust particle sizes are presented in the Table 1, for an 11μm strip of cold welded

interface.

| Height (um) | Dust Particle number |
|---|---|
| 0 to 0.02 | 0 |
| 0.02 to 0.04 | 5 |
| 0.04 to 0.06 | 3 |
| 0.06 to 0.08 | 1 |
| 0.08 to 0.10 | 1 |
| 0.10 to 0.12 | 4 |

Table 1.1: Sample distribution μm of dust particles along an 11μm strip of the cold welded interface [21]

TEM and Electron Energy Loss Spectroscopy (EELS) analyses were used to study the typical irregularity/void formed along the cold-welded interface [37]. The TEM images are shown in Figure 2.10. These show the locations that were used for the EELS analyses. The comparison of EELS results collected from these locations (across the Au-Ag cold welded interface) is presented in Fig. 2.8. This shows that there was a clear increase in both carbon and silver peaks in the irregularity/void position (position 2).

However, only gold or silver peaks were found in the other two locations (Positions 1 and 3). These results suggest that a carbon-rich dust particle was trapped in position 2. The dust particles are most likely native to clean-room, [34]. The experimental evidence of an "S"-shape contact is in agreement with earlier work by Cao [34] that considered the effects of dust particles on the stamping of organic electronic devices.

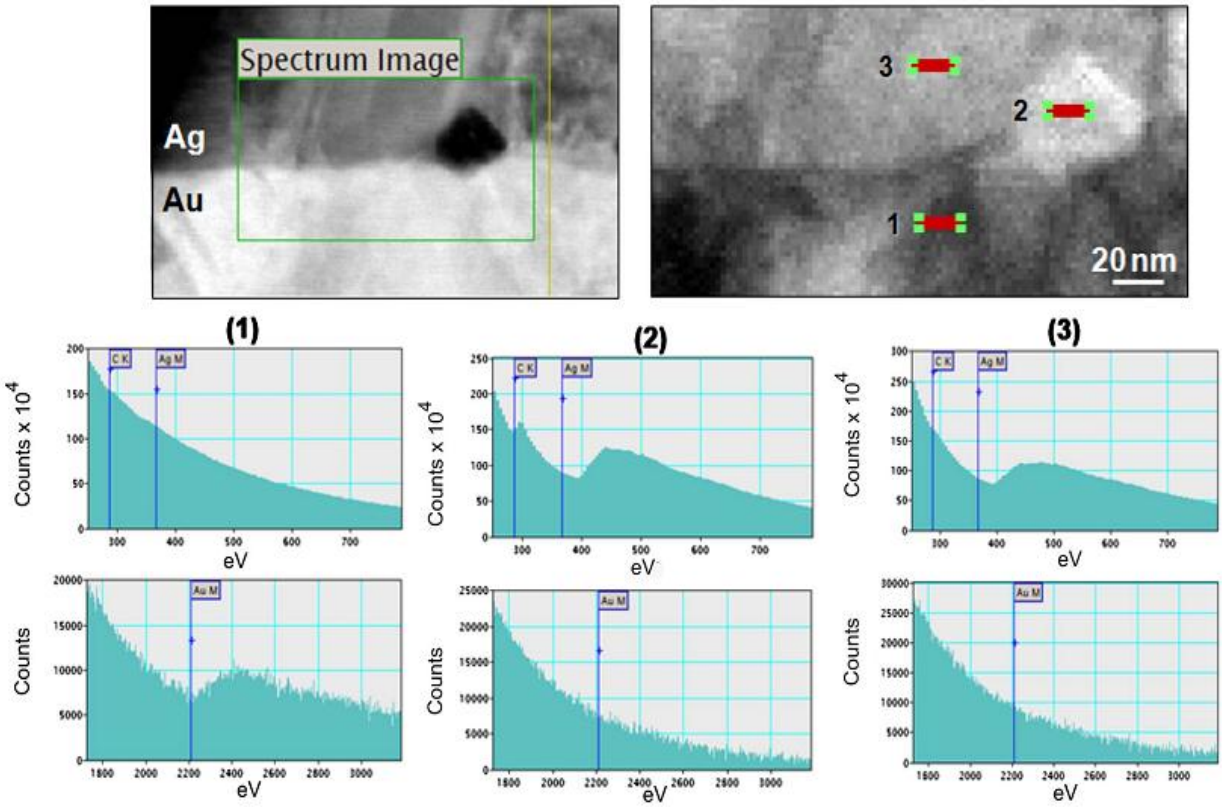


Figure 2.10: The TEM images showing the locations nearby the cold-welded interface for doing the electron energy loss spectroscopy (EELS); Comparison of EELS collected from various locations across the Au-Ag cold welded interface show there is a clear increase in both carbon and silver peaks in Position 2 [37]

**2.5 Material Transport across Interfaces**

In an effort to understand the possible material transport that can occur during cold welding process [38], the areal densities of Au and Ag were obtained using EELs. These were plotted against distance within various strip regions across the Au-Ag cold welded interface, as shown in Fig. 2.11. Note that although diffusion process could possibly occur in strip 1 and strip 2, since Au and Ag are directly in contact with each other, there is no possibility for inter diffusion to occur in the region contained within strip 3, in which void is present between the Au and Ag surfaces [37].

The widths of the composition slopes in strips 1 and 2 (9.5nm and 7.7nm respectively) are also very close to those within strip 3 (7.7nm for either surface). This suggests that the compositional profiles (across the cold weld interfaces) are not diffusion. Otherwise, the widths of the composition slopes in strips 1 and 2 would be much different from those in strip 3. Hence, the current widths of the composition slopes are attributed to the effects of the intermixing that occur during the cold welding of the Au-Ag interface.

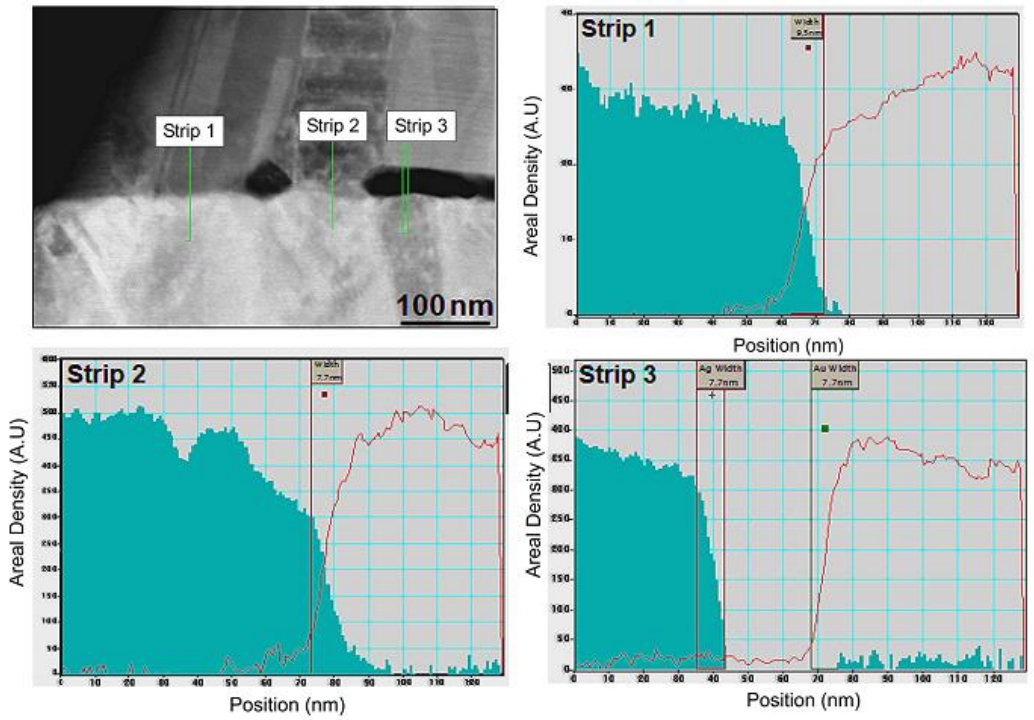


Fig. 2.11: Comparison of EELs collected from various strip regions across the Au-Ag cold welded interface [37]

## 2.6 Theory of Adhesion

Adhesion is the tendency of two dissimilar materials to cling together. It is a result of attractive forces which can either be chemical, dispersive, or diffusive in nature. In chemical adhesion, two materials form a compound through ionic, covalent, or hydrogen bonding at the interface. In dispersive adhesion, Van der Waals forces form polar attractions between

two molecules while in diffusive adhesion, mobile or soluble molecules travel across the interface, that join the two materials together. Hence, the strength of adhesion refers to the energy required to break these adhesive bonds, which dependent on both the strength and number of bonds that are formed (i.e. contact surface area).

In order to determine the energy required to separate these dissimilar materials, various adhesion models exist (Figure 2.12) which takes into account, the different materials and geometric properties of the interacting layers. The classical Hertzian contact theory [39] assumed that there is no adhesion between two elastic spheres in contact. The Johnson-Kendall-Roberts (JKR) model [40] describes the contact between soft materials with short range, strong adhesion forces, and large tip radii. On the other hand, the Derjaguin-Muller-Toporov (DMT) model [41] applies to adhesion between stiff materials with long range, weak adhesion forces, and small tip radii.

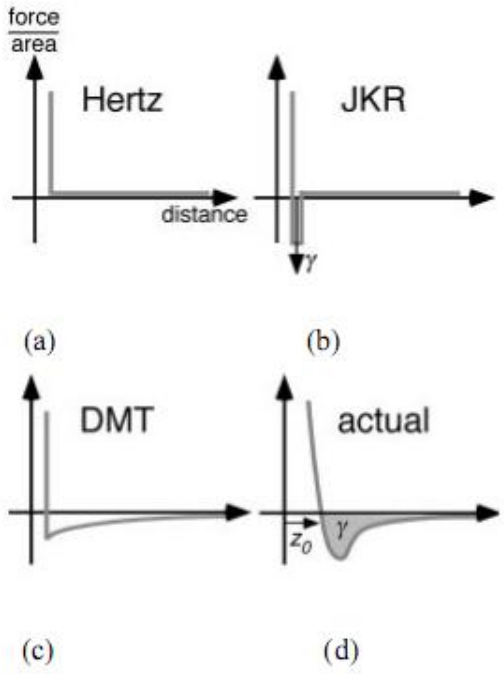


Figure 2.12: Interaction forces (per unit area) for (a) Hertz model, (b) JKR model, (c) DMT model and (d) actual interaction [43].

In these methods, the adhesion forces can be estimated by the following two limiting cases: the Johnson-Kendall-Roberts (JKR) model [40], which applies in the case when the adhesion forces are short range compared to the elastic deformation they produce (i.e. compliant material with strong adhesion), and the Derjaguin-Muller-Toporov (DMT) model [41], which describes the case of long range surface forces with a Hertzian geometry (i.e. stiff materials, weak adhesion forces). The Maugis-Dugdale (MD) model is intermediate between the JKR and DMT models, [42] which proposes an analytical solution.

The force-distance relation in the Maugis-Dugdale (MD) model is shown in Figure 2.13 [43], which is an analytical solution in the intermediate regime between the JKR and DMT models. Maugis [42] used a Dugdale square well potential to approximate the interaction potential in reality. In this interaction, a constant adhesive stress (force per unite area) $\sigma_o$ acts between the surfaces over a range of $\delta_t$. Thus, the work of adhesion, i.e. adhesion energy, can be calculated as;

$$\gamma = \sigma_o \delta_t \qquad 2.1$$

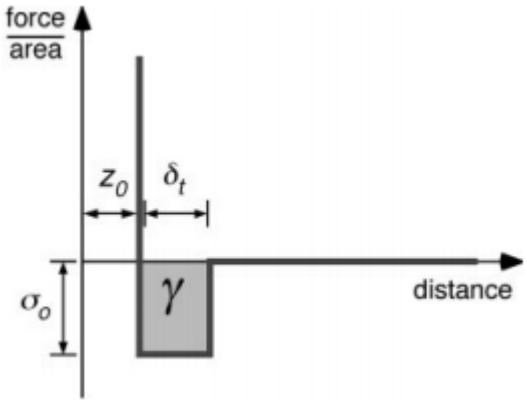


Fig. 2.13: Schematic of Dugdale model used by Maugis [43].

To select the appropriate model, Maugis [39] defined a transition parameter, λ, which is given by:

$$\lambda = 2\sigma_o \left(\frac{R}{\pi\kappa^2\gamma}\right)^{\frac{1}{3}} \qquad 2.2$$

where $\lambda$ is the adhesion energy per unit area;

R is the combined radius given by;

$$R = \frac{R_1 R_2}{R_1 + R_2} \qquad 2.3$$

where $R_1$ and $R_2$ are the radii of the two spheres, respectively; $\kappa$ is the combined elastic modulus for two spheres in contact, which is given by ,

$$\kappa = \frac{4}{3}\left[\frac{(1-\nu_1)^2}{E_1} + \frac{(1-\nu_2)^2}{E_2}\right] \qquad 2.4$$

$E_1$ and $E_2$ are the elastic moduli of the two spheres, and $\nu_1$, $\nu_2$ are the Poisson ratios of the two spheres, respectively. By choosing $\sigma_o$ to match the minimum adhesive stress of a Lennard-Jones potential with equilibrium separation distance $z_o$, it follows that $\delta_t = 0.97 z_o$. The JKR model applies when $\lambda > 5$, while the DMT model applies when $\lambda < 0.1$. The MD model is applicable to the intermediate values of λ.

In the non-zero adhesion cases, the negative critical load at which the surfaces of two spheres separate, when being pulled apart, was defined as pull-off force or adhesion force. For the two extreme cases, it is given in JKR and DMT theories by:

$$F_{JKR} = \frac{3}{2}\pi\gamma R \qquad 2.5$$

and;

$$F_{DMT} = 2\pi\gamma R \qquad 2.6$$

In the MD model, two equations are needed to relate the contact radius, a, and the contact force, F:

$$\frac{\lambda \hat{a}^2}{2}\left[\sqrt{m^2-1}+(m^2-2)cos^{-1}\left(\frac{1}{m}\right)\right]$$

$$+\frac{4\lambda^2\hat{a}}{3}\left[\sqrt{m^2-1}cos^{-1}\left(\frac{1}{m}\right)-m+1\right]=1 \qquad 2.7$$

and;

$$\hat{F} = \hat{a}^3 - \lambda\hat{a}^2\left[\sqrt{m^2-1}+m^2cos^{-1}\left(\frac{1}{m}\right)\right] \qquad 2.8$$

where $\hat{a}$ and $\hat{F}$ are two dimensionless parameters defined by:

$$\hat{a} = \frac{a}{\left(\frac{\pi\gamma R^2}{\kappa}\right)^2} \qquad 2.9$$

$$\hat{F} = \frac{F}{\pi\gamma R} \qquad 2.10$$

and the parameter m represents the ratio between the contact radius, a, and an outer radius, c, when the gap between the sphere surfaces reaches δt , i.e., where the adhesion no longer takes place.

Meanwhile, the above equations are difficult to use, because there is no single expression relating only a and F. Equations (2.7) and (2.8) need to be solved simultaneously by letting m vary appropriately between limits, which depend upon λ. Furthermore, in the usual case with experimental measurements, such as AFM force measurement, the value of λ is an unknown. The relation for the pull-off force must be determined through an iterative technique [41]. The relation between contact radius a and the contact radius at zero load $a_{0,}$ that was proposed by Carpick et al. [43], can be described by a generalized equation

$$\frac{a}{a_o} = \left( \frac{\alpha + \sqrt{1 - {F}/{F_{ad}}}}{1 + \alpha} \right)^{\frac{2}{3}} \qquad 2.11$$

$F_{ad}$ is the general adhesion force. When $\alpha = 1$, it corresponds exactly to the JKR case, and when $\alpha = 0$ , it corresponds exactly to the DMT case. They showed that for intermediate cases, for which $0 < \alpha < 1$, the generalized transition equation corresponds very closely to solutions provided by Maugis using the Dugdale model. By curve fitting, they also provided a conversion equation from α to λ, i.e.

$$\lambda = -0.924 ln(1 - 1.02\alpha) \qquad 2.12$$

Equation (2.12) was later modified by Pietrement and Troyon [45] through fitting to be

$$\lambda = -0.913 ln(1 - 1.018\alpha) \qquad 2.13$$

Applying Equation (2.10) to adhesive forces gives;

$$F_{ad} = \frac{F_{ad}}{\pi\gamma R} \qquad 2.14$$

They also determined empirical equation that give direct conversion equations between parameters α and $F_{ad}$ by:

$$F_{ad} = 0.267\alpha^2 - 0.767\alpha + 2.000 \qquad 2.15$$

The AFM force measurement measures $F_{ad}$. If R and K are known, the adhesion energy can be calculated by solving the Equations (2.2), (2.13), (2.14) and (2.15).

The above studies suggest that the adhesion and contact inside and between each layer of the organic electronic devices are crucial to the performance and the lifetime of OLEDs and organic electronic structures in general. It has also been suggested by Jeng et al. [46] that the surface roughness of the layers in the organic electronic devices influences the injection of hole-carriers. Since the injected current is dominated by the tunneling of hole-carriers at low bias, increasing the effective contact area at the interfaces lowers the barrier to the hole injection in the devices. Hence, there is a need to study the fundamental physics of adhesion and contact and their roles in the organic electronic devices. The resulting insights could clearly lead to the future design of OLEDs and organic electronic structures with improved performance and longer lifetime.

Zong et al. [47] presented a study of adhesion energies that are relevant to Au-Au microswitch contacts at both the nano- and micron-scales. The micronscale adhesion measurements were obtained from cantilever beam bending measurements and fracture mechanics models. The nanoscale adhesion measurements were achieved by AFM pull-off

experiments and adhesion theory models. The adhesion energies obtained for both methods were found to be in good agreement.

Tong et al. [48] also used similar AFM force measurement techniques to measure the adhesion forces between materials relevant to organic solar cells and organic light-emitting devices. The contact pairs included organic-organic, organic-inorganic, and inorganic-inorganic interfaces. The measured pull-off forces and surface parameters were then incorporated into theoretical models for the estimation of surface energies. The results can be used to identify either interfaces with weak adhesion, that need to be modified to reduce the chances of failure, or interfaces with strong adhesion, that would be good candidates for organic electronic devices. However, the use of such adhesion energies in interfacial contact has not been fully explored. There is, therefore, a need to integrate the measurements of adhesion energy with interfacial contact models in a way that will improve the performance the OLED structures.

**References**

1. Zur et al, “Organic Light-emitting Diodes with Doped Charged Transport Layers” Ph.D. Thesis, Dresden (2001)

2. M. Pope, H. P. Kallmann, and P. Magnante, “Electroluminescence in Organic Crystals,” The Journal of Chemical Physics, vol. 38, no. 8, p. 2042, (1963)

3. C. W. Tang and S. A. VanSlyke, “Organic electroluminescent diodes,” Applied Physics Letters, vol. 51, no. 12, p. 913, (1987)

4. W. Helfrich, W. G. Schneider, “Phys. Rev. Lett., 14 (1965) 229-231

5. J.H. Burroughes, D.D.C. Bradley, A.R. Brown, R.N. Marks, K. Mackay, R.H. Friend, P.L. Burns, A.B. Holmes. Nature, 347 (1990) 539–541

6. J. M. Shaw and P. F. Seidler, “Organic electronics: Introduction,” IBM Journal of Research and Development, vol. 45, no. 1, pp. 3-9, Jan. (2001)

7. Y. Xia, J. a. Rogers, K. E. Paul, and G. M. Whitesides, “Unconventional Methods for Fabricating and Patterning Nanostructures,” Chemical Reviews, vol. 99, no. 7, pp. 1823-1848, Jul. (1999)

8. Y. Xia and G. M. Whitesides, “Soft lithography,” Angewandte Chemie International Edition, vol. 37, no. 5, pp. 550-575, Mar. (1998)

9. Y. Xia and G. M. Whitesides, “Soft lithography,” Annual Review of Materials Science, vol. 28, no. 1, pp. 153-184, Aug. (1998)

10. J. Rhee and H. H. Lee, “Patterning organic light-emitting diodes by cathode transfer,” Applied Physics Letters, vol. 81, no. 22, p. 4165, (2002)

11. C. W. Joo, S. O. Jeon, K. S. Yook, and J. Y. Lee, “Improved device performances in polymer light-emitting diodes using a stamp transfer printing process,” Organic Electronics, vol. 10, no. 2, pp. 372-375, Apr. (2009)

12. C. Kim, Y. Cao, W. O. Soboyejo, and S. R. Forrest, “Fabrication of organic light-emitting devices by direct transfer of active organic materials using organic-organic adhesion,” in The 17th Annual Meeting of the IEEE Lasers and Electro-Optics Society, 2004. LEOS 2004, (2004), vol. 1, pp. 336-337.

13. T. W. Lee, J. Zaumseil, Z. Bao, J. W. P. Hsu, and J. A. Rogers, “Organic light-emitting diodes formed by soft contact lamination.,” Proceedings of the National Academy of Sciences of the United States of America,” vol. 101, no. 2, pp. 429-33, Jan. (2004)

14. J. Ouyang and Y. Yang, “Conducting polymer as transparent electric glue,” Advanced Materials, vol. 18, no. 16, pp. 2141-2144, Aug. (2006)

15. T. Zyung, S. H. Kim, H. Y. Chu, J. H. Lee, S. C. Lim, J.-I. Lee, and J. Oh, “Flexible organic LED and organic thin-film transistor,” Proceedings of the IEEE, vol. 93, no. 7, pp. 1265-1272, Jul. (2005)

16. H. Liu and R. Sun, “Laminated active matrix organic light-emitting devices,” Applied Physics Letters, vol. 92, no. 6, p. 063304, (2008)

17. G. H. Kim, J. Oh, Y. S. Yang, L.-M. Do, and K. S. Suh, “Lamination process encapsulation for longevity of plastic-based organic light-emitting devices,” Thin Solid Films, vol. 467, no. 1-2, pp. 1-3, Nov. (2004)

18. J. H. Kim, S.-min Seo, and H. H. Lee, “Nanovoid nature and compression effects in organic light emitting diode,” Applied Physics Letters, vol. 90, no. 14, p. 143521, (2007)

19. H. Czichos, “The Mechanism of the Metallic bond,” J. Phy D: Appl Phys, 5, 1890-1897 (1972)

20. Ken Gilleo, Area Array Packaging Materials: Adhesives, Pastes, and Lead-Free, Mc-Graw-Hill Professional, New York, (2003)

21. N. Bay, “Cold Pressure Welding – The Mechanism Governing Bonding,” Journal of Engineering for Industry, 101, 121-127 (1979)

22. C. Kim, P. E. Burrows, and S. R. Forrest, “Micropatterning of Organic Electronic Devices by Cold-welding,” Science, 288, no. 5467, 831-833, (2000)

23. Adhesion or Cold Welding of Materials in Space Environments, ASTM, (1967)

24. X. Xu, M. Davanco, X. Qi, and S. R. Forrest, “Direct transfer patterning on three dimensionally deformed surfaces at micrometer resolutions and its application to hemispherical focal plane detector arrays,” Organic Electronics, vol. 9, no. 6, pp. 1122-1127, Dec. (2008)

25. C. Kim, M. Shtein, and S. R.Forrest, “Nanolithographic based on Patterened Metal transfer and its Application to organic electronic devices,” Appl. Phys. Lett. 80, 4051, (2002)

26. G. Ferguson, M. K. Chaudhury, G. B. Sigal and G. M. Whitesides, “Contact Adhesion of Thin Gold-films on Elastomeric Supports-Cold Welding under ambient Conditions,” Science, 253, no. 5021, 776 – 778, (1991)

27. N. A. Alcantar, C. Park, J. M. Pan, and J. N. Israelachvili, Acta Mater., 51, 31-47, (2002)

28. C. Kim, Patterning of Organic Electronic Devices. Princeton, NJ: Princeton University, Ph.D. Thesis, (2005)

29. M. Iordachescu, J. Iordachescu, J. Planas, E. Scutelnicu, J. L. Ocana, “Material Flow and Hardeningat butt Cold Welding of Aluminium,” Journal of Materials Processing Technology, Volume 209, Issue 9, 1 May 209, Pages 4255-4263

30. R. F. Tylecote, “Investigations on Pressure Welding,” British Welding Journal, 1, 117-135 (1954)

31. S. Jeon, V. Malyarchuk, J. O. White, and J. A. Rogers, “Optically Fabricated three dimensional Nanofluidic Devices,” Nano Letters, 5, 1351-1356 (2005)

32. W. Zhang and N. Bay, “Cold Welding – Theoretical Modeling of the Weld Formation” Journal, 76, 47 (1997)

33. W. Y. Zhang, G. S. Ferguson and S. Tatic-Lucic, Elastomer-Supported Cold Welding for room Temperature wafer-Level Bonding Proceedings of IEEE International Conference in Micro electro Mechanical systems, 741-744 (2004)

34. Y. Cao, C. Kim, S. R. forrest, and W. O. Soboyejo, "Effect of Dust Particles and Layer Properties on Organic Electronic Devices Fabricated by Stamping," Journal of Applied Physics, 98. no. 3, 033 713-1, (2005)

35. C. Kim and S. R. Forrest, "Fabrication of Organic-Light Emitting Devices by Low Pressure Cold Welding," Advanced Materials, 15, no. 6, 541-545, (2003)

36. Y. Cao, N. Yao, K. McIlwrath, J. Zhou, G. Osinkolu, and W. O. Soboyejo, "An investigation of Au-Ag interface formed by cold welding using focused ion beam/transmission electron microscopy," in MRS Proceedings, (2011), vol.965, pp. 1-6.

37. W. O. Akande, Y. Cao, N. Yao, and W. Soboyejo, "Adhesion and the Cold Welding of Gold-Silver Thin Films" Journal of applied Physics, 107, 043519 (2010)

38. A. J. Kinloch, Adhesion and Adhesives: Science and Technology (Chapman and Hall, London, (1987)

39. V. H. H. Hertz, "Ueber die Berührung fester elastischer Körper," Journal für die reine und angewandte Mathematik (Crelle's Journal), no. 92, pp. 156-171, (1882)

40. K. L. Johnson, K. Kendall, and A. D. Roberts, "Surface energy and the contact of elastic solids," Proceedings of the Royal Society A: Mathematical, Physical and Engineering

Sciences, vol. 324, no. 1558, pp. 301-313, Sep. (1971)

41. B. Derjaguin, “Effect of contact deformations on the adhesion of particles,” Journal of Colloid and Interface Science, vol. 53, no. 2, pp. 314-326, Nov. (1975)

42. D. Maugis, “Adhesion of spheres: The JKR-DMT transition using a Dugdale model,” Journal of Colloid and Interface Science, vol. 150, no. 1, pp. 243-269, Apr. (1992)

43 R. Carpick, D. Ogletree, and M. Salmeron, “A general equation for fitting contact area and friction vs load measurements,” Journal of Colloid and Interface Science, vol. 211, no. 2, pp. 395-400, Mar. (1999)

44. M. A. Lantz, S. J. O’Shea, M. E. Welland, and K. L. Johnson, “Atomic-force-microscope study of contact area and friction on NbSe2,” Physical Review B, vol. 55, no. 16, pp. 10776-10785, Apr. (1997)

45. O. Piétrement and M. Troyon, “General equations describing elastic indentation depth and normal contact stiffness versus load,” Journal of Colloid and Interface Science, vol. 226, no. 1, pp. 166-171, Jun. (2000)

46. T. W. Lee, J. Zaumseil, Z. Bao, J. W. P. Hsu, and J. A. Rogers, “Organic light-emitting diodes formed by soft contact lamination,” Proceedings of the National Academy of Sciences of the United States of America, vol. 101, no. 2, pp. 429-33, Jan. (2004)

47. Zong Zong, Yifang Cao, Nima Rahbar, and Wole Soboyejo, “Nano and Micro Scale Adhesion Energy Measurement for Au-Au contacts in micro switch structures,”

J. Applied Physics 100, 104313 (2006)

48. T. Tong, B. Babatope, S. Admassie, J. Meng, O. Akwogu, W. Akande, and W. O. Soboyejo, “Adhesion in organic electronic structures,” Journal of Applied Physics, vol. 106, no. 8, p. 083708, (2009)

## Chapter 3

## 3.0 Analytical and Computational Modeling of Contact and Adhesion

### 3.1 Device Architecture

Organic light emitting diodes (OLEDs) are layered structures that consist of sequential organic layers that are stacked between a metallic cathode and an inorganic anode as shown in Figure 3.1. The device is usually built on a transparent substrate (such as glass) that finally forms the display through which the emitted light is observed. A thin film of indium tin oxide (ITO) is sputtered on the substrate, which forms the anode of the device. ITO is frequently used because of its high conductivity and transparency that allow sufficient light to be transmitted from the device [1]. On top of the ITO anode, is a thin layer of poly(3, 4-ethylene dioxythiophene) that is doped with poly(styrenesulfonate) (PEDOT:PSS). This is a conducting polymer that is used to facilitate hole injection from the anode into the active layer. This material tends to have better hole injection than bare ITO [1]. It is deposited on the ITO as hole injection layer (HIL), rather than a stand-alone electrode. The photo-emissive active layer of the OLED is deposited on PEDOT:PSS. This is the layer in which electrons and holes supplied by the cathode and anode recombine to generate light. One of the common materials that are used to form the active layer is poly[2-methoxy-5-(2'-ethyl-hexyloxy)-p-phenylenevinylene] (MEH:PPV). This has a molecular weight between 150,000 and 250,000 [2]. It produces a reddish-orange light with a peak emission around 550 nm. To complete a device, gold can be cold-welded on the gold or silver with a pattern (~ 50- 150 nm thick) of Au-Au or Au-Ag that forms the cathode layer.

Under the action of a driving voltage of a few or a coupled of volts, electrons are injected from a metal cathode with a low work-function into the electronic state corresponding to the lowest unoccupied molecular orbital (LUMO) of a conjugated polymer; holes are injected

from a bilayer anode (PEDOT:PSS on ITO) into the electronic state corresponding to the highest occupied molecular orbital (HOMO) of a conjugated polymer [1]. Both electrons and holes, coming from different electrodes, move from opposite directions towards the recombination zone, where they can combine to form excitons. This leads to a population of excited states of the emissive polymers that subsequently emits light.

Cold welding [3] is one of the low cost OLED fabrication processes that can be used to join metallic materials. In additive cold welding (as shown in Figure 2.6 in the previous chapter), the material that is being transferred is first deposited onto a patterned stamp. This is then pressed onto the substrate at a prescribed pressure and temperature. In additive cold welding, material that is being transferred from the stamp to the substrate is left behind on the substrate when the stamp is lifted.

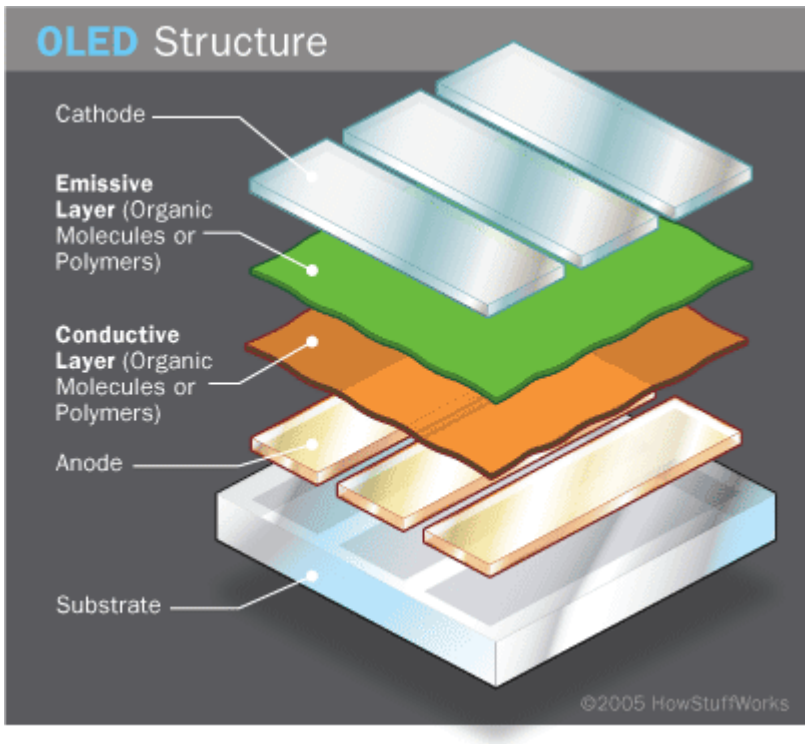


.

Figure 3.1: Schematic of OLED

In this work, published data for the materials that were used in the model OLED structures as shown in Figures 3.2 were obtained. These were incorporated into finite element models that were used for the simulation of the cold welding technique. The models explored the effects of applied pressure on the cold welding structures with dust particles at the interfaces between adjacent layers. The results show the influence and significance of pressure on the contact and deformation of these layers around dust particles or impurities in the clean room environment. The implications of the results are discussed for the fabrication of OLEDs by cold welding.

### 3.2 Analytical Modeling of Contact and Adhesion

We model the cold welding process between gold and silver in the presence of dust particle as shown in Figure 3.2 a and b. This is analogous to a cantilever deflection on a rigid particle that is described in Figure 3.3. This figure shows the elastic deformation of the beam around the dust particle. The presence of the dust particle (as shown in Figure 3.2(a)) restricts the attractive adhesive forces between the two approaching surfaces. Hence, the adhesive forces act initially on the dust-free areas between the approaching surfaces. Furthermore, depending on the elastic nature of the dust particle and that of the beam, the beam can bend around the dust particle or the dust particle can be flattened completely by the weight of the beam [4]. In the current work, it is assumed that the elastic properties of the dust particle fall within the requirements of the former circumstance. In other words, the dust particle is assumed to be rigid enough to cause bending under uniform pressure.

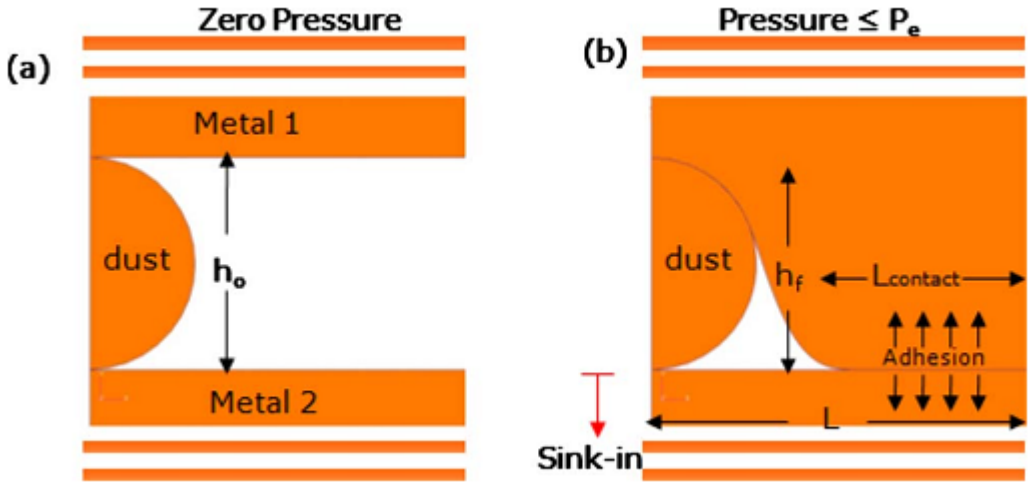


Figure 3.2: Cold welding in the presence of dust particles. (a) Initial approach of the two surfaces to be pressure welded with the dust particle embedded on the surface of metal 2. (b) Metal elastically deforms around the dust particle [4]

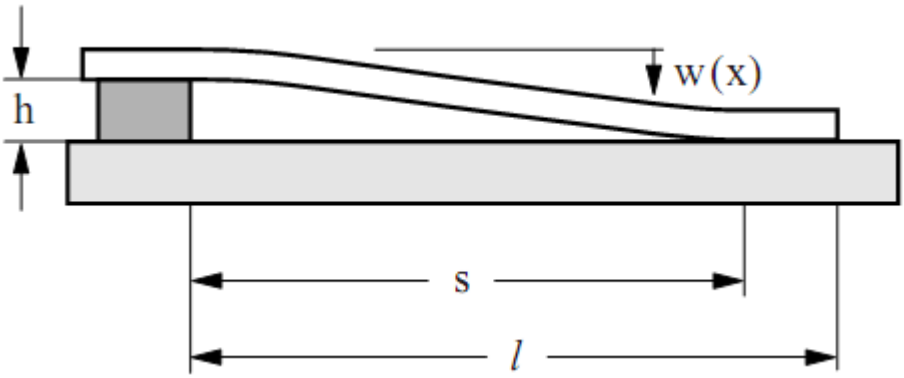


Figure 3.3: The adhesive contact for a cold-welding model consisting of a thin, elastic beam and a base

The differential equation of a beam in this case is given as:

$$\frac{d^4w}{dx^4} = 0 \qquad 3.1$$

Its solution fulfills the boundary conditions: $w(0) = 0, w(s) = h, w'(0) = 0\ and\ w'(s) = 0.$ This yields the following solutions:

$$w(x) = \frac{h}{s^3}(3x^2 s - 2x^3) \quad 3.2$$

$$w'(x) = \frac{h}{s^3}(6xs - 6x^2) \quad 3.3$$

$$w''(x) = \frac{h}{s^3}(6s - 12x) \quad 3.4$$

$$w''(x)^2 = \frac{h^2}{s^6}(36s^2 - 144sx + 144x^2) \quad 3.5$$

The elastic energy of the beam can be calculated using;

$$U_{el} = \int_0^s \frac{1}{2} EIw''(x)^2 dx \quad 3.6$$

$$= \frac{1}{2} EI \frac{h^2}{s^6} \int_o^s (36s^2 - 144xs + 144x^2) dx \quad 3.7$$

$$\therefore U_{el} = \frac{6EIh^2}{s^3} \quad 3.8$$

The earlier work by Zong et al [5] has shown that, the total energy of the system is the sum of the elastic energy stored in the beam (due to the bending) and the surface energy.

$$i.e.\ U_s = \frac{6EIh^2}{s^3} - \gamma(l - s)a \quad 3.9$$

Where $a$ and E are the width and Young's Modulus of the beam respectively, $\gamma$ is the adhesion energy, I is the second moment of area of the beam and $l$ is the length of the beam (Figure 3.3).

The single minimum value of the total energy of the system occurs at a corresponding equilibrium value of s (for s <$l$) which can be expressed as:

$$\frac{dU_s}{ds} = \frac{-18EIh^2}{s^4} + \gamma a \qquad 3.10$$

At equilibrium, $\frac{dU_s}{ds} = 0$.

Hence, from equation 4.7, we can write the following expression;

$$\gamma a = \frac{18EIh_f^2}{s^4} \qquad 3.11$$

where the second moment of inertia is: $I = \frac{at^3}{12}$. Substituting the analytical form of I into equation 3.11 gives the surface energy at equilibrium as;

$$\gamma = \frac{3}{2}\frac{Et^3h_f^2}{s^4} \qquad 3.12$$

This implies that;

$$s = S_{s-shape} = \left(\frac{3}{2}\frac{Et^3h^2}{\gamma}\right)^{\frac{1}{4}} \qquad 3.13$$

This shows that the void length can be calculated from the dust particle heights. Equation 3.3 implies that if the geometries and the modulus of the cantilever beam in the structure are known, one can determine the adhesion energy. On the other hand, AFM pull-off technique can be used to measure adhesion energy, such that void length can be determined. It can also be inferred that, if the length of the beam is smaller than s, it can not "remain stuck" to the base. Akande et al. [4] described a simple condition that ensures that the contact is s-shaped (and not) for any given dust particle height.

This is illustrated as:

$$l \geq S_{arc} + S_{shape} \tag{3.15}$$

Hence, the sufficient condition is

$$l \geq \left[1 + \frac{1}{\sqrt{2}}\right] S_{s-shape} \tag{3.16}$$

Therefore, $l \geq 1.7 S_{shape}$ or $l \sim 2 S_{shape}$ (3.17)

The analysis above can be represented by Figure 3.4 below, where we consider layer of length, L, and void length, S, together with contact length Lc.

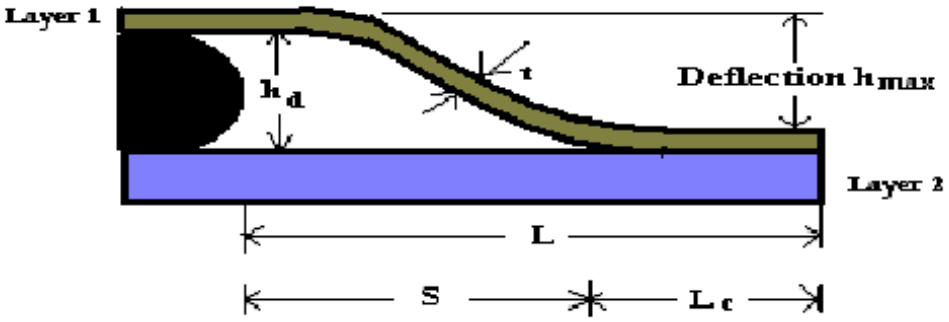


Figure 3.4: Schematic of Contact and Void lengths

This implies that:

$$L_c = L - S \tag{3.18}$$

$$\therefore \frac{L_c}{L} = 1 - \frac{S}{L} \tag{3.19}$$

$$i.e. Contact\ Length\ ratio = 1 - Void\ Length\ ratio \tag{3.20}$$

Hence, equations 3.13 and 3.19 were used to investigate the relationships between: (1) the contact length and adhesion at different thicknesses, (2) void length and adhesion at different moduli, and (3) contact length and adhesion at different moduli.

### 3.3 Finite Element Modeling

This work examines the effects of pressures on the cold welding of metals that are relevant to organic light emitting diodes. Finite element simulations of the cold welding process were conducted using the ABAQUS software package. ABAQUS CAE 6.12 (teaching edition) was used in the simulations. It was used in modeling the cold welding of gold on silver and that of silver on gold. The effects of dust particles' moduli as well as thickness of the layers on the effective contact length were also considered in the simulations.

The work of Akande et al. [4] has shown the presence of carbon-rich dust particles in the clean room environment whose sizes ranges from 0.02 μm to 0.20 μm. Moreau et al. [6] and [7] have also shown that dust particles exist in the clean room environment. They include: silicon, iron, aluminum, quartz, textile polymer, silicone and photoresist. The dust particles are described by Kim et al. [8] as mostly native to the clean-room. Usually, during the cold welding processes, the dust particles are interposed between the stamp and the substrate. They, therefore, affect the development of the contact areas between the approaching layers. Cao et al. [9] have shown that, in the cold welding processes, soft stamps are expected to deform easily around such dust particles at relatively low pressures. Meanwhile, considerably higher pressures are needed to deform stiff stamps over similar contact areas.

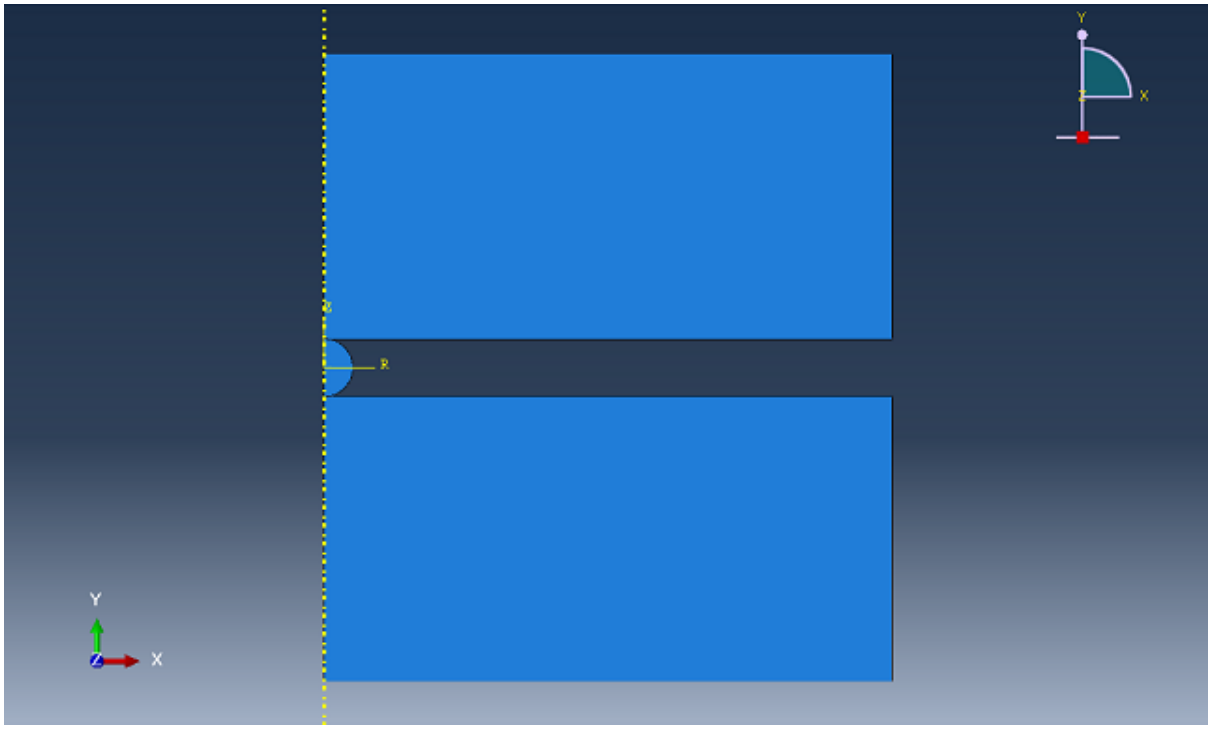


Figure 3.5: Geometry of the cold welding model

The cylindrical geometry of the devices was simplified using axisymmetric shell geometries. A typical geometrical model of the materials is shown in Figure 3.5. This shows a gold-coated stamp about to be cold welded onto a silver layer in the vicinity of dust particle. The dust particle diameter was chosen to be 10 nm. Considering the work of Akande et al. [4], which reported carbon-rich dust particle in the interface between gold and silver during cold welding, the Young's modulus used in the first modeling was 10.2 GPa (Young's modulus for Carbon). This was used to study the ratio of contact length to the total length as a function of the applied pressure. Subsequently, other possible values of moduli were considered, which take care of rigid, semi-rigid and compliant dust particles. Likewise, the contact length ratio was examined as a function of thickness of the materials to be cold welded.

Four-node bilinear axisymmetric quadrilateral elements were used in the mesh. The mesh was also biased towards the edge of the surfaces that contain the dust particle. This ensures that the mesh is dense in the regions near the dust particle and the regions near the surface

contact regimes. The meshing was analyzed using plane strain conditions. All the materials that were used, were assumed to exhibit isotropic elastic behavior. The Young's moduli and the Poisson ratio were obtained from the prior studies by Cao et al [9], Bietsch et al [10], Soboyejo [11] and Cambridge Engineering Selector (CES) [12].

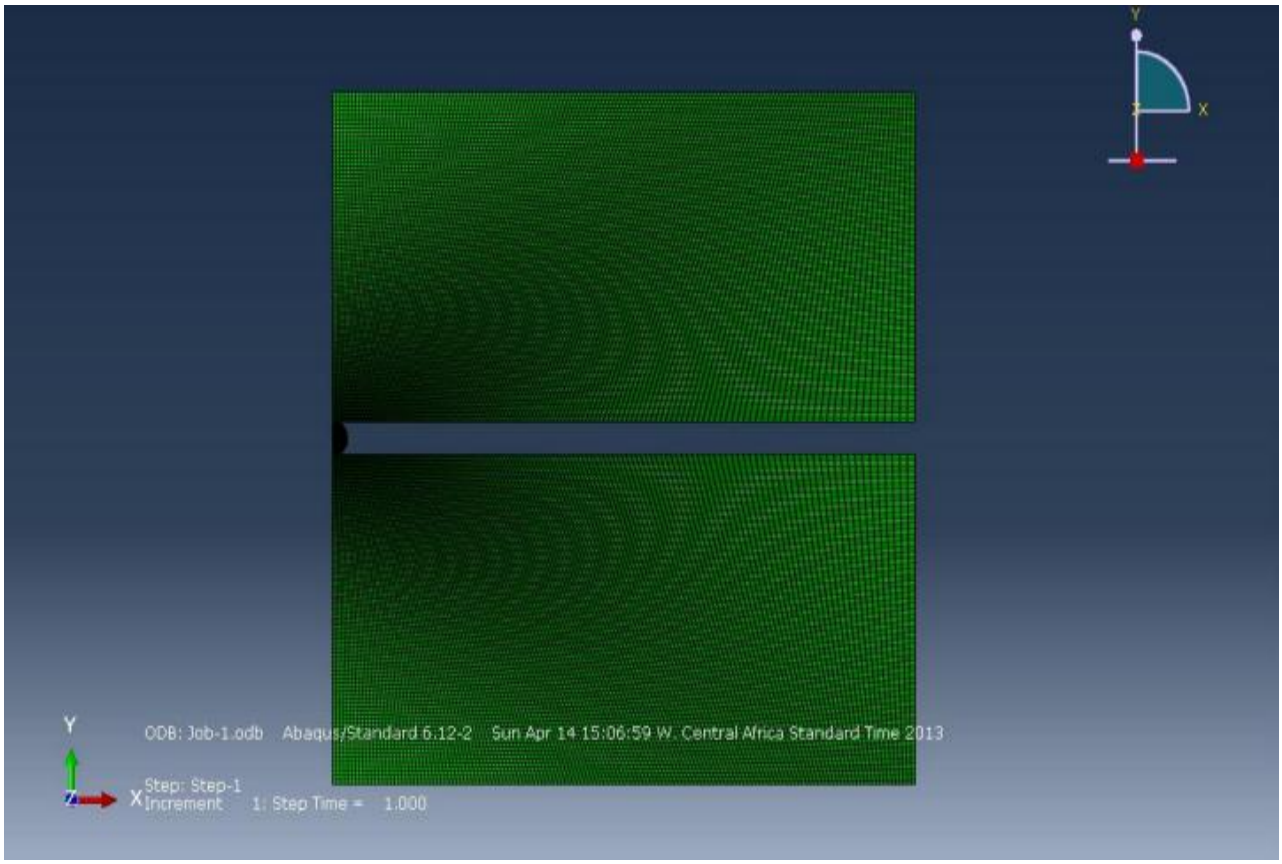


Figure 3.6: Meshing of the geometry

The Young's moduli and Poisson's ratios of the materials used in the simulation were summarized in Table 3.1 below:

| Materials | Young's Modulus E (GPa) | Poisson Ratio, v | Reference |
|---|---|---|---|
| Gold (Au) | 82.00 | 0.42 | Ref. [9] [11] & [12] |
| Silver (Ag) | 76.00 | 0.40 | Ref. [11] & [12] |
| Carbon | 10.30 | 0.23 | Ref. [12] |
| Aluminum (Al) | 70.00 | 0.30 | Ref. [10] |
| Polyethylene (low density) | 0.20 | 0.30 | Ref. [11] & [12] |

Table 3.1: Summary of FEA input parameters

Frictionless contact was assumed between the dust particle and the stamp, and also between the dust particle and the substrate. This was done for simplicity and convergence in the finite element simulations. However, rough contacts were used for the two approaching layers [2]. This was used to cater for adhesive interactions between the substrate and the stamping materials. This ensured that there was no relative sliding, after the substrate and the stamping materials were brought into contact.

The axisymmetric boundary condition (BC1) was applied at the symmetry axis and the lowest part of the substrate was fixed to have no displacement and rotation (BC2) as shown in Figure 3.7 below. Also, the outer edge of the model was fixed to have no lateral movement for continuity. Then, the top of the stamp moved downward, as a result uniformly distributed pressure that was applied to the uppermost part of the stamp.

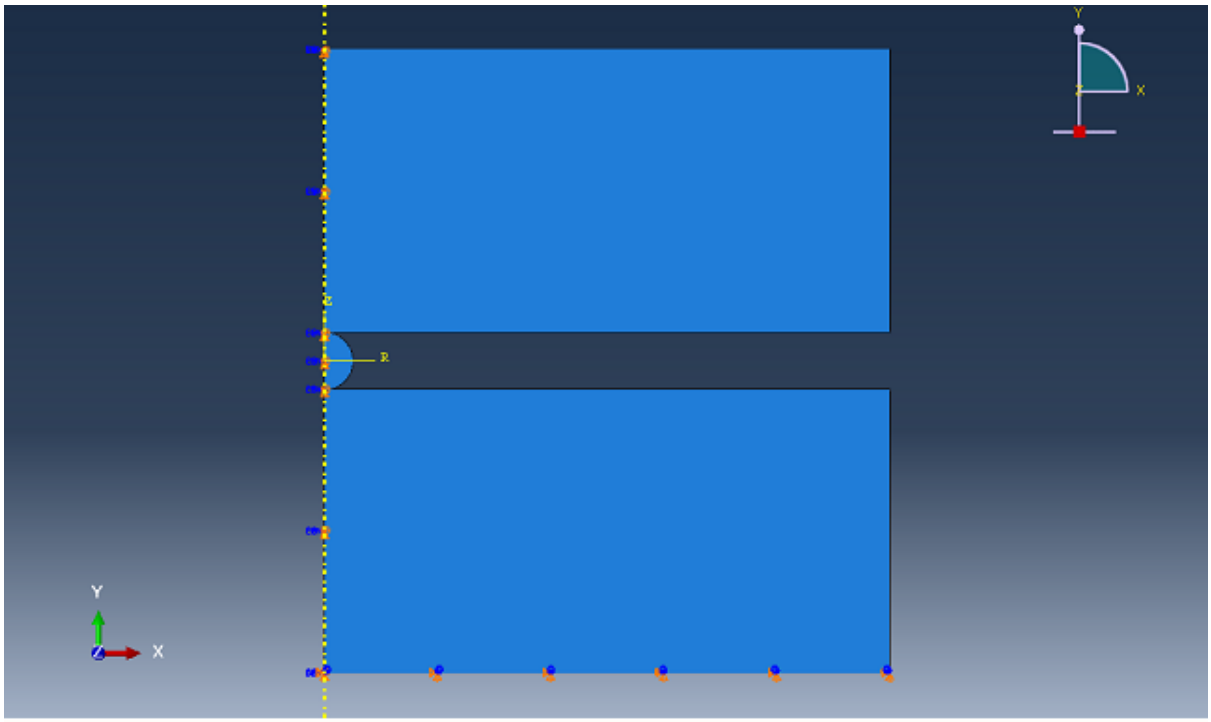


Figure 3.7: Implementing boundary conditions onto the model

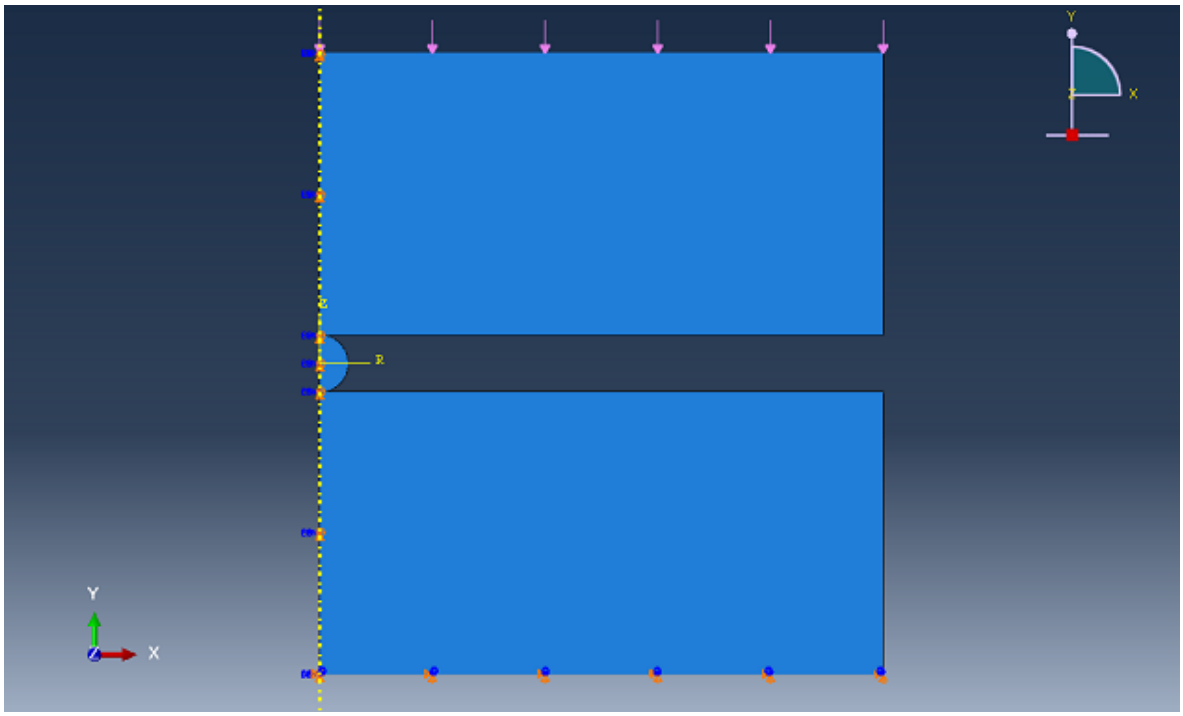


Figure 3.8: Application of uniformly distributed pressure

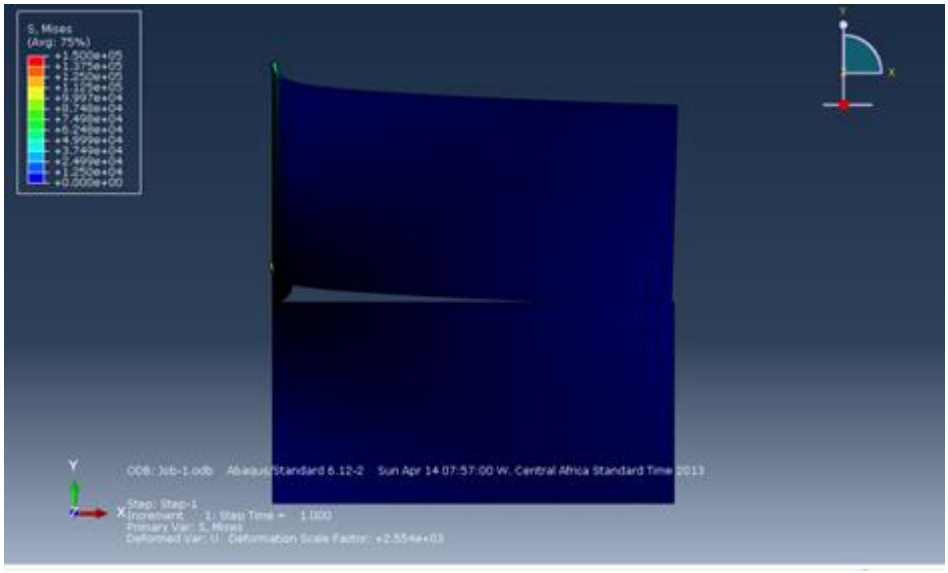


Figure 3.9: Deformed profile for cold welding of gold on silver at a pressure of 50KPa

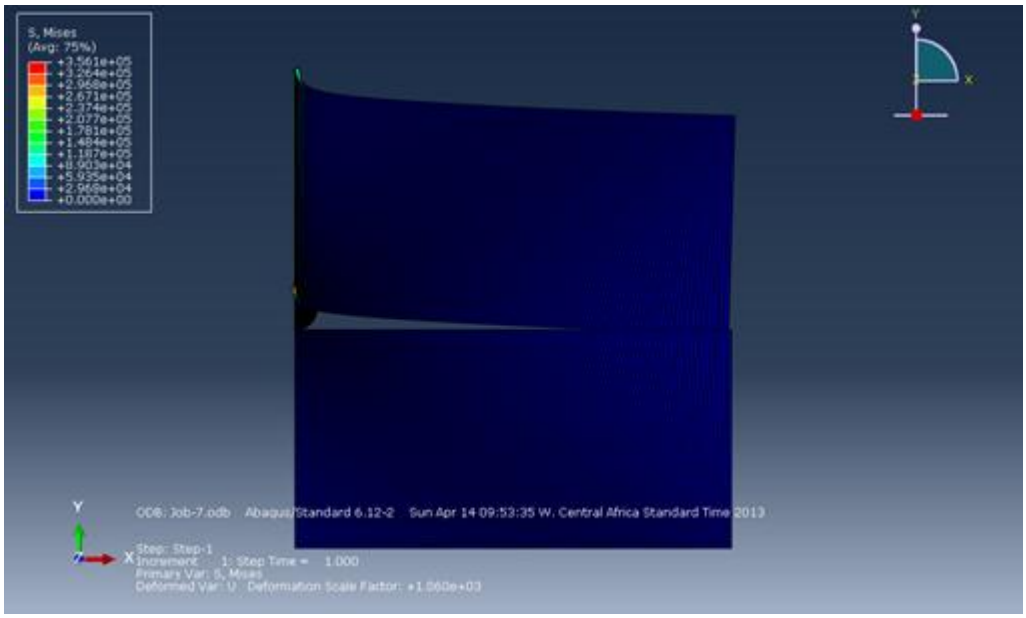


Figure 3.10: Calculated deformed profile for cold welding of silver on gold at a pressure of 50KPa

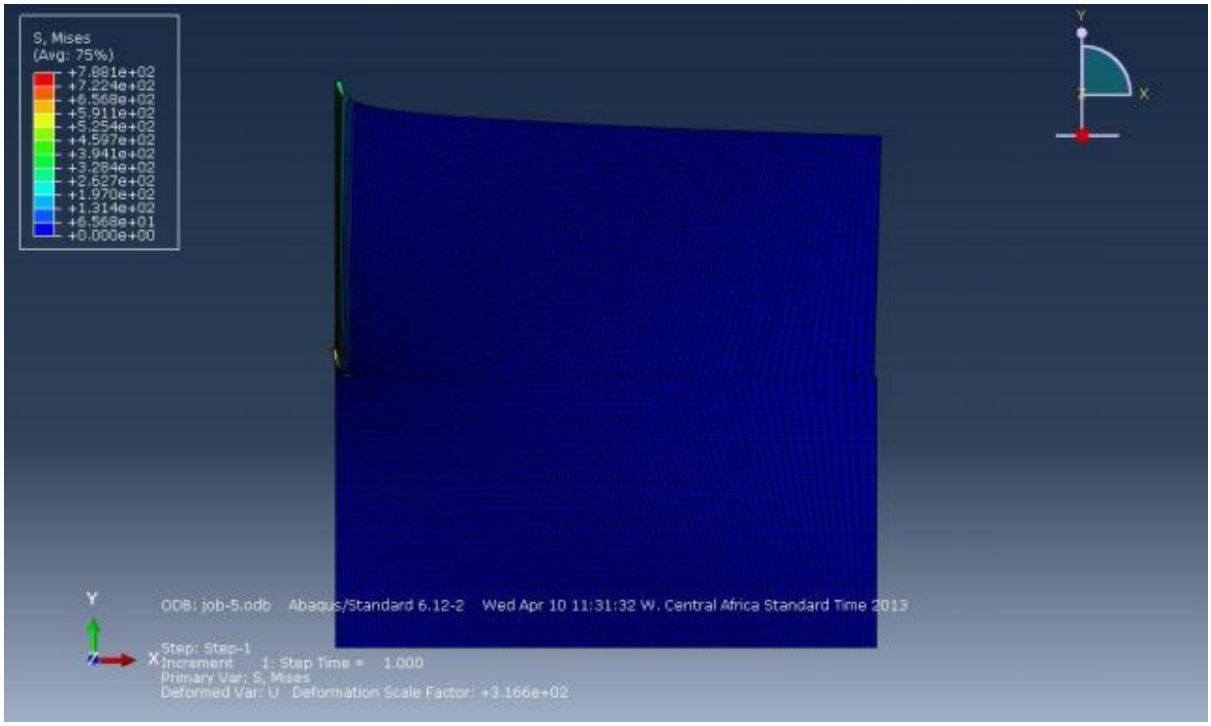


Figure 3.11: Deformed profile of the compliant particle

# Chapter 4

## Results and Discussion

### 4.1 Analytical Results and Discussion

The results of the analytical modeling discussed in chapter 3 are presented in this section. The results are presented in graphical forms for better appreciation. The plots were obtained and plotted through codes written (as shown in appendix) with the Matrix Laboratory software (MATLAB, Version R2009b, MathWorks Inc., Natick, Massachusetts, USA).

#### 4.1.1 Plot of Contact Length as a function of Adhesion Energy for Different Thicknesses

$$s = S_{s-shape} = \left(\frac{3}{2}\frac{Et^3h^2}{\gamma}\right)^{\frac{1}{4}} \quad 4.1$$

$$Since, L_c = L - S \quad 4.2$$

$$\therefore \frac{L_c}{L} = 1 - \frac{S}{L} \quad 4.3$$

Figure 4.1 shows increase in contact length as the adhesion energy increases for the three different layer thicknesses under consideration. The contact length, however, is greatest for the thin layer and lowest for the thickest layer. The adhesion energy of 30 J/m$^2$ for instance, corresponds to about 50% contact length in the layer with 150 nm thickness (thickest layer in this work). However, the same energy value results to about 80% contact length for layer with 50 nm thickness (thin layer).

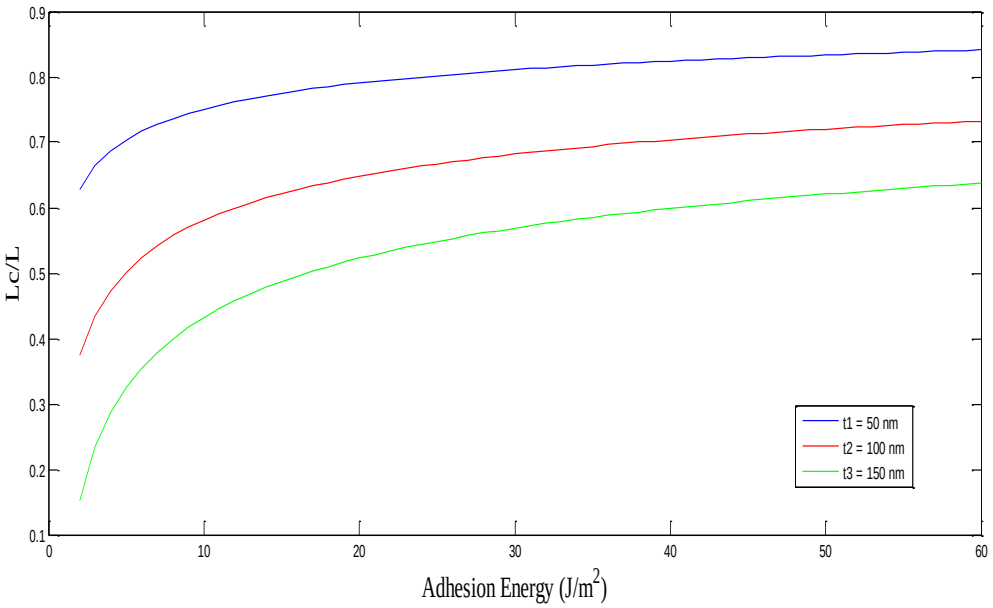


Figure 4.1: Plot of Contact Length against Adhesion Energy for Different Thicknesses

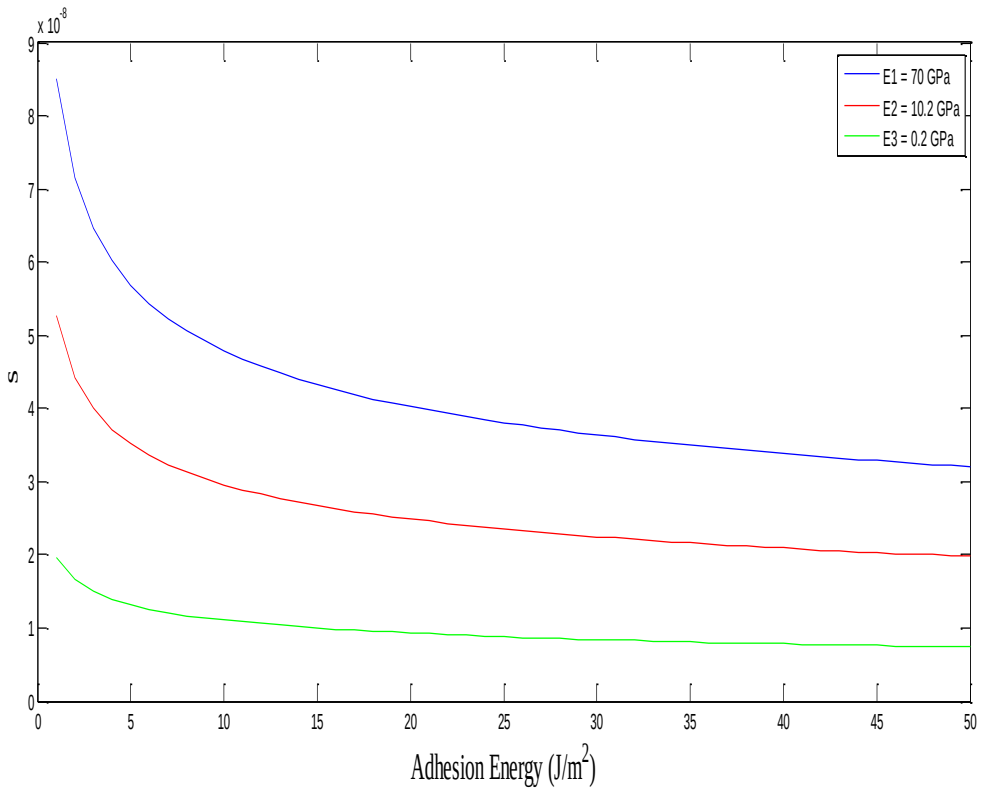


Figure 4.2: Plot of Void Length against Adhesion Energy for Different Moduli

### 4.1.2 Plot of Void Length as a function of Adhesion Energy for Different Moduli

Equation 4.1 was also considered in writing the codes for the above heading. Figure 4.2 above shows decrease in void length as the adhesion energy increases for the three different particles moduli. The moduli, which are: 70 GPa, 10.2 GPa and 0.2 GPa. These represent rigid, semi-rigid, and compliant particles, respectively, in this work. The void length, however, is greatest in the case of rigid particle, moderate in the semi-rigid particle, and lowest in the compliant particle for all values of the adhesion energy.

### 4.1.3 Plot of Contact Length as a Function of Adhesion Energy for Different Moduli

Figure 4.3 below, on the other hand, shows increase in contact length as the adhesion energy increases for the three different particles' moduli. The contact length is greatest in the compliant particle, moderate in the semi-rigid particle, and lowest in the rigid particle for all values of the adhesion energy.

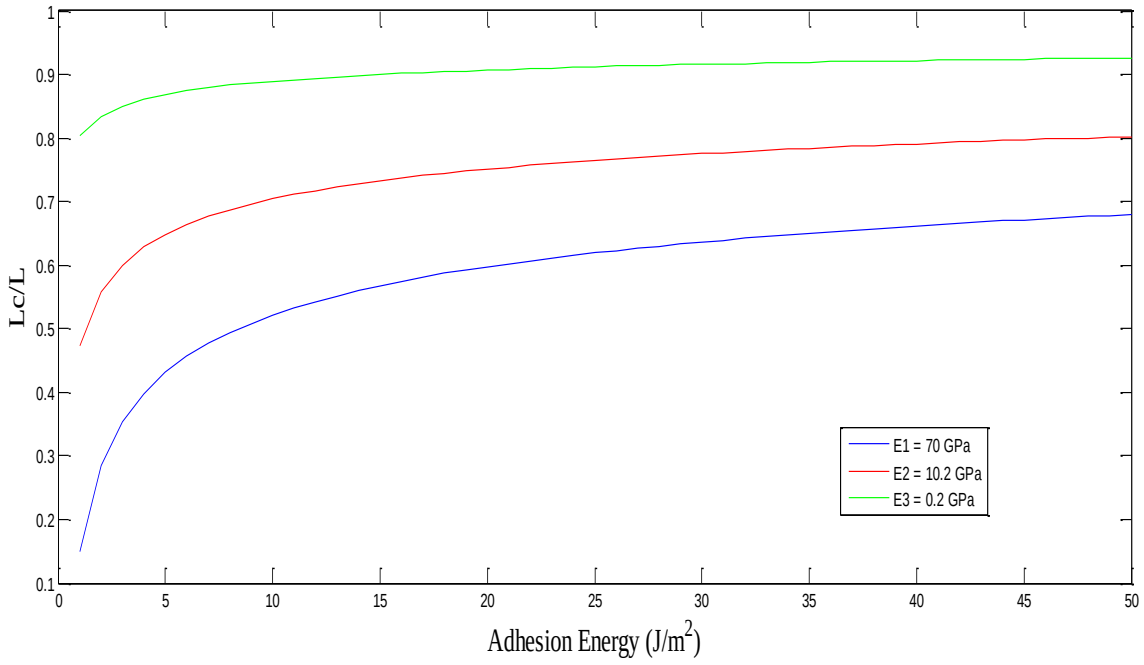


Figure 4.3: Plot of Contact Length against Adhesion Energy for Different Moduli

## 4.2 Finite Element Analyses (FEA) Results and Discussions

### 4.2.1 Effects of Pressure on the Contact length

Figure 3.9 (as shown in chapter 3) shows the typical deformed profiles of a gold-coated stamp on a silver coated substrate, while Figure 3.10 shows that of a silver-coated stamp on a gold-coated substrate deformed under pressure. The stamps have obviously deformed around the dust particles and thereby made contact with the substrates. The performance of the cold welding process can be described by the ratio of the contact length, Lc, to the total length, L. This is illustrated in Figure 4.4, in which the contact length ratio is plotted against the applied pressure, for both gold on silver (Au on Ag) and silver on gold (Ag on Au). The plots (Figure 4.4) show increase in the contact length (for both Au on Ag and Ag on Au) as the applied pressure is increased. However, the contact length ratios reach plateau as the pressures are increased above a certain level.

Furthermore, the contact of silver on gold results in a slightly higher contact length ratio than the contact of gold on silver. The minimum pressure required to attain the plateau contact length ratios is approximately 220 kPa. This corresponds to about 80% contact length ratio for Au on Ag and about 83% contact length ratio for Ag on Au. The contact length ratio remains relatively equal in both cases beyond this pressure value. Increase in pressure beyond this 220kPa leads to sink-in of the materials which could damage the device. The above optimum pressure value recorded in this work is in close agreement with the earlier experimental work by Kim et al. [8] who recorded approximately 180 kPa for the critical pressure required for cold welding of gold using PDMS. It is, however, important to note the higher contact length ratio of silver compared to that of gold at equal applied pressures. This is consistent with the fact that gold is stiffer than silver, based on their respective moduli.

Also, Akande et al. [4] have reported a higher adhesive force for Ag on Au than that for Au on Ag. These are responsible for the discrepancy in the contact length ratios.

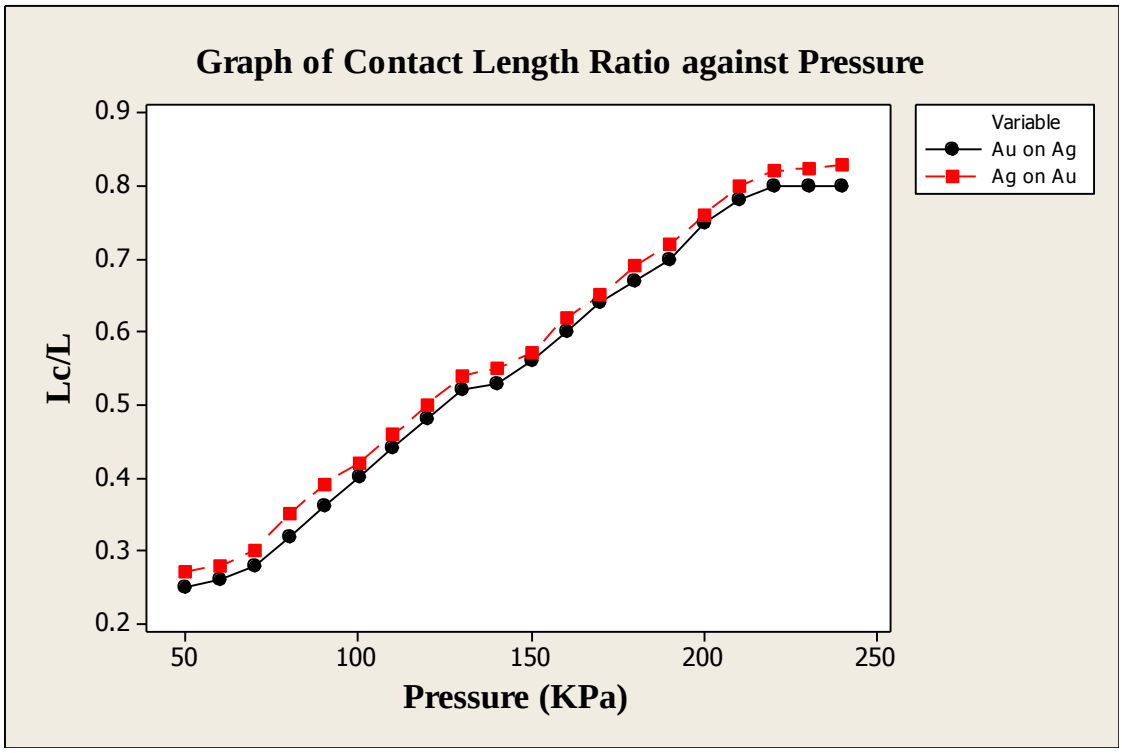


Figure 4.4: Plot of Contact Length ratio against Pressure for Au on Ag and Ag on Au

### 4.2.2 Effects of dust particle's modulus

The presence of dust particles and their effects on the performance of organic electronics has been reported by Akande et al. [4], Kim et al [8] and Cao et al [9]. However, less attention has been paid to the effect of dust particle moduli in a way that shows its effect on the fabrication and performance of OLEDs devices. Hence, it is important to investigate the effects of dust particles moduli that are relevant to the fabrication of organic electronic structures. The current work examines a rigid, semi-rigid and compliant dust particle. The rigid material examined is aluminum; the semi-rigid is carbon while the compliant material is low density polyethylene. These particles have Young's moduli of 70 GPa, 10.2 GPa and 0.2 GPa respectively. The plot (Figure 4.5) below shows that the compliant material with

modulus of 0.2 GPa resulted in high levels of contact length ratio, while the rigid particle with modulus of 70 GPa has the least level of contact length ratio. The semi-rigid particle on the other hand has an intermediate contact length ratio, compared to that of rigid and compliant particles. This illustrates the dominant role that the hardest particle plays in the contact between the layers during cold welding.

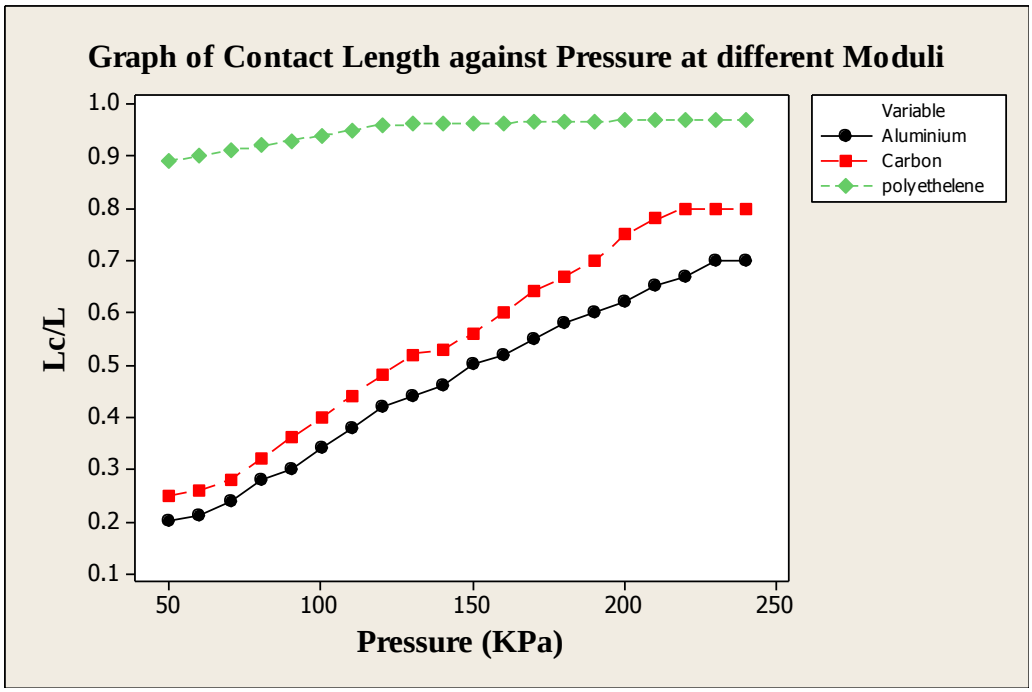


Figure 4.5: Plot of Contact Length Ratio against Pressure at Different Moduli

### 4.2.3 Effects of layer thickness

The significance of using soft stamps for cold welding of organic electronic structures has been demonstrated by Kim et al. [8] and Cao et al. [9]. However, the effects of the transfer layer thickness are yet to be explored. This work reveals that thinner layers give rise to higher contact length ratios. This is shown in Figure 4.6 in which a pressure of 200 kPa resulted in ~80% contact length ratio, for a 50 nm contact layer thickness. However, the same pressure resulted to ~50% contact length ratio for a 150 nm contact layer thickness. This implies that,

for stiffer materials, the effective contacts dependent mainly on the overall stiffness of the structure, as suggested by Du et al. [2].

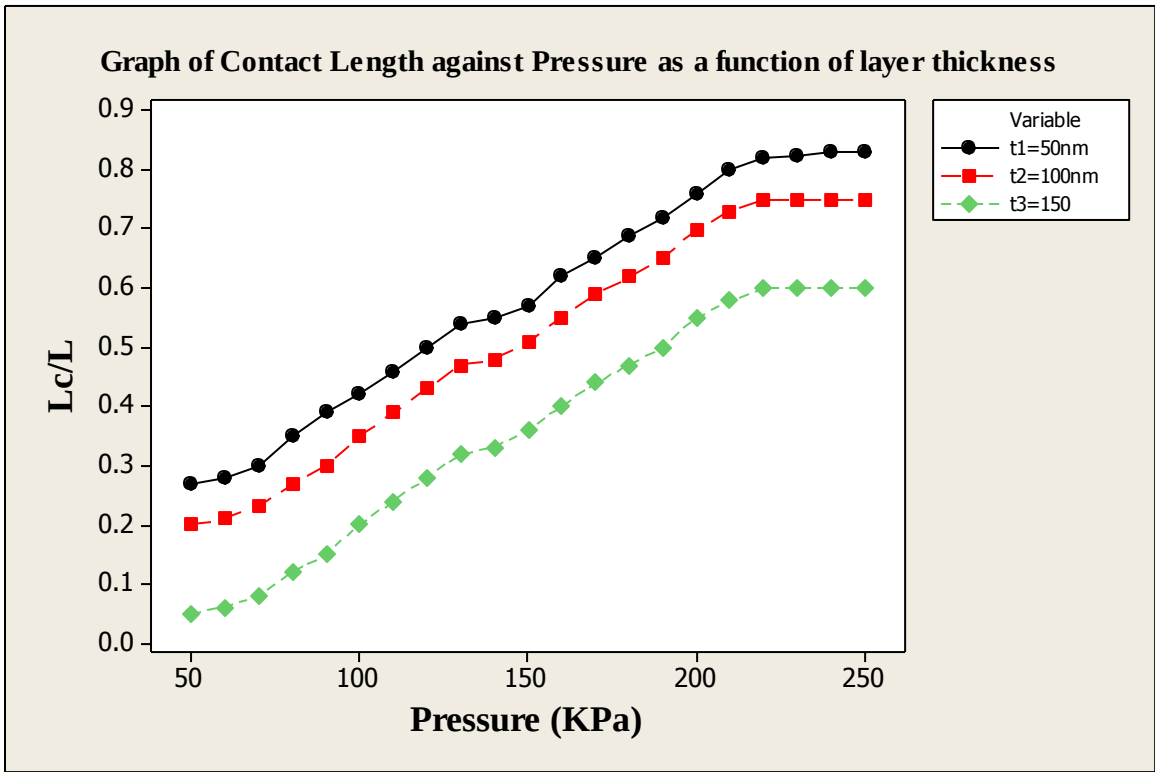


Figure 3.12: Plot of Contact Length against Pressure as a Function of Layer Thickness

### 4.3 Implications

The implications of the above analytical and computational models are quite important for the fabrication of organic electronic structures via cold welding. The results suggest that the contact areas in such situation will depend strongly on the applied pressure during the process and the adhesion energies between the contacting surfaces. The improved contact could enhance the successful transfer of the cold welding material. This could also improve the electronic properties of the cold welding devices. Meanwhile, excessive pressure (beyond the required minimum value) could result in sink-in and damage to the devices.

The current work also shows that the moduli of the dust particles that are present in the clean room can also significantly affect the contact. Compliant particles result in improved contact

and adhesion, as shown by both the analytical results in Figures 4.2 and 4.3 and the finite element analysis results in Figure 4.5. If the dust particles are stiffer, the layers will wrap around them and adhere in regions away from the dust particles. This elastic wrapping of the layer can facilitate the formation of voids, which could eventually compromise charge transport, performance, and the fabrication yield of organic electronic devices.

Also, the selection of layer thickness should be done in a way that will improve the contact length ratio. Usually, the thicker layer results in a device with increased stiffness and reduced contact i.e. increased void length. Conversely, the thinner layer results in a device with improved contact and adhesion. Hence, the latter should result in improved electronic properties. Further work is needed to determine the optimum film layer thickness with the best balance of stiffness and contact for application in organic electronic structure.

## References


1. Sam-Shajing Sun, “Introduction to Organic Electronics and Optoelectronic Materials and Devices” (2008).
2. J. Du, T. Tong, W. Akande, A. Tsakiridou and W. Soboyejo “Pressure effects on the lamination of organic light emitting devices,” under review.
3. C. Kim, P. E. Burrows, and S. R. Forrest, “Micropatterning of Organic Electronic Devices by Cold-welding,” Science, vol. 288, no. 5467, pp. 831-833, May (2000).
4. W. Akande et. al. “Adhesion and the cold welding of gold-silver thin films,” J. Appl. Phys. 107, 043519 (2010).
5. Zong, Z. et al. (2006), “Nano- and microscale adhesion energy measurement for Au–Au contacts in microswitch structures”- Journal Of Applied Physics 100, 104313
6. W. M. Moreau, Semiconductor Lithography: Principles, Practices, and Materials. New York: Plenum Press, (1988).
7. International Organization for Standardization, ISO 14644-1:1999 Cleanrooms Of, and Associated Controlled Environments-Part I: Classification of Air Cleanliness, vol. 1999. Switzerland: ISO, (1999).
8. C. Kim and S. Forrest, “Fabrication of organic light-emitting devices by low-pressure cold welding,” Advanced Materials, vol. 15, no. 6, pp. 541-545, (2003).
9. Y. Cao, C. Kim, S. R. Forrest, and W. Soboyejo, “Effects of dust particles and layer properties on organic electronic devices fabricated by stamping,” Journal of Applied Physics, vol. 98, no. 3, pp. 033713-033713-6, (2005).
10. A. Bietsch and B. Michel, “Conformal contact and pattern stability of stamps used for soft lithography,” Journal of Applied Physics, vol. 88, no. 7, p. 4310, (2000).
11. W. Soboyejo, Mechanical Properties of Engineered Materials. New York: CRC, (2003).
12. Cambridge Engineering Selector Edupack, (CES), (2008).

# Chapter 5

# Conclusion and Recommendation

## 5.1 Conclusion

This work presents the results of a combined analytical and computational study of the cold welding of Au and Ag thin films that are relevant to stamping processes that are being explored for the fabrication of organic electronic structures. The geometries of the materials used in this work and their (published) mechanical properties are incorporated into the analytical and finite element simulations of the cold welding process. These were used to study the effect of pressure, adhesion, particle's modulus, as well the layer thickness.

The result suggests that a required or appropriate pressure is needed to balance the cold welding device efficiency and damage of the device. The current work also shows that contact length increases with increase in adhesion energy. The thinner layer shows greater contact even at lower pressure, with less damage to the device. Meanwhile, thinner films are less stable structurally. This implies that an optimized film thickness has to be determined.

Furthermore, the simulations reveal the significance of dust particle modulus as it affects the contact length during cold welding. Both the analytical and computational models show that the compliant particle results in improved contact length, while the rigid particle results in elastic wrapping of the layer which could limit the contact and facilitate distribution of voids. This could eventually compromise charge transport, performance, and the fabrication yield of organic electronic devices.

## 5.2 Recommendations

In order to extend and improve the results of this work, the following steps are suggested for possible future work:

1. The possible sink-in that occurs during cold welding should be studied with finite element analysis.
2. The simulations should also be carried out through atomic scale simulations. This will facilitate better understanding of the possible intermixing and other processes that occur during cold welding at atomic scale.
3. Experimental work should be carried out to validate the results of the present work.

## Appendices

### A1 Codes for Contact Length against Adhesion at different thicknesses

```
clear all
close all
%%%%%%%%%%%%%%%%%%%%%%%%%%%%%%%%%%%%%%%%%%%%%%%%%%%%%%%%%%%%%%%%%%%%%%%%%%%%%%%%
%%%%%%%%%%% Codes for the Contact against Adhesion %%%%% S. A. ADENIJI %%%%
%%%%%%%%%%%%%%%%%%%%%%%%%%%%%%%%%%%%%%%%%%%%%%%%%%%%%%%%%%%%%%%%%%%%%%%%%%%%%%%%

          t1=5.00*10^-8;                    % Thickness of layer 1
          t2=1.00*10^-7;                    % Thickness of layer 2
          t3=1.50*10^-7;                    % Thickness of layer 3
          l=2.0*10^-7;                      % Length of the layer

          E=8.2*10^10;                      % Young's modulus of Au

          h=0.2*10^-8;                      % height of the particle

          b1=((3/2)*t1^3*E*h^2);          % Constant for s-shape (thickness 1)
          b2=((3/2)*t2^3*E*h^2);          % Constant for s-shape (thickness 2)
          b3=((3/2)*t3^3*E*h^2);          % Constant for s-shape (thickness 3)

          p=2:1:60;                         % adhesions
          s1=zeros(1,size(p,2));
          s2=zeros(1,size(p,2));
          s3=zeros(1,size(p,2));
          for n=1:size(p,2);
              s1(n)=(b1*(1/p(n)))^(1/4);     % Void's length for s-shape 1
              s2(n)=(b2*(1/p(n)))^(1/4);     % Void's length for s-shape 2
              s3(n)=(b3*(1/p(n)))^(1/4);     % Void's length for s-shape 3
          end
          %lc=l-s
          lc1=l-s1;                           % Contact length for s-shape 1
          lc2=l-s2;                           % Contact length for s-shape 2
          lc3=l-s3;                           % Contact length for s-shape 3
          z1=lc1/l;                           % Lengths ratio for s-shape 1
          z2=lc2/l;                           % Lengths ratio for s-shape 2
          z3=lc3/l;                           % Lengths ratio for s-shape 3
          %plot(p,s,'b-'); hold on
          %plot(p,s1,'r-'); hold on
          plot(p,z1,'b-'); hold on
          plot(p,z2,'r-'); hold on
          plot(p,z3,'g');hold on
```

## A2 Codes for Void Length and Contact Length against Adhesion at Different Moduli

```
clear all; close all
%%%%%%%%%%%%%%%%%%%%%%%%%%%%%%%%%%%%%%%%%%%%%%%%%%%%%%%%%%%%%%%%%%%%%%%%%%%%
%%%% Codes for the void length and contact length against adhesion%%%%%%
%%%%%%%%%%%%%%%%%%%%%%   S. A. ADENIJI %%%%%%%%%%%%%%%%%%%%%%%%%%%%%%%%%%%%
%%%%%%%%%%%%%%%%%%%%%%%%%%%%%%%%%%%%%%%%%%%%%%%%%%%%%%%%%%%%%%%%%%%%%%%%%%%%

          t=5.0*10^-8;           % Thickness of the layer

          l=1.0*10^-7;           % Length of the layer

          E1=7.0*10^10;          % Young's modulus of rigid particle
          E2=1.02*10^10;         % Young's modulus of semi-rigid particle
          E3=0.2*10^9;           % Young's modulus of compliant particle
          h=0.2*10^-8;           % height of the particle

          b1=((3/2)*t^3*E1*h^2); % Constant for s-shape for rigid particle
          b2=((3/2)*t^3*E2*h^2); % Constant for s-shape for semi-rigid part.
          b3=((3/2)*t^3*E3*h^2); % Constant for s-shape for compliant part.

          p=1:1:50;              % adhesions
          s1=zeros(1,size(p,2));
          s2=zeros(1,size(p,2));
          s3=zeros(1,size(p,2));
          for n=1:size(p,2);
              s1(n)=(b1*(1/p(n)))^(1/4);     % Void's length for rigid
              s2(n)=(b2*(1/p(n)))^(1/4);     % Void's length for semi-rigid
              s3(n)=(b3*(1/p(n)))^(1/4);     % Void's length for compliant
          end

          %lc=l-s
          lc1=l-s1;               % Contact length for rigid particle
          lc2=l-s2;               % Contact length for semi-rigid particle
          lc3=l-s3;               % Contact length for compliant particle
          z1=lc1/l;               % Lengths ratio for rigid particle
          z2=lc2/l;               % Lengths ratio for semi-rigid particle
          z3=lc3/l;               % Lengths ratio for compliant particle
          plot(p,s1,'b-'); hold on
          plot(p,s2,'r-'); hold on
          plot (p,s3,'g-');hold on
          %plot(p,z1,'b-'); hold on
          %plot(p,z2,'r-'); hold on
          %plot(p,z3,'g-'); hold on
```